Monthly Notices
of the
ROYAL ASTRONOMICAL SOCIETY

Mon. Not. R. Astron. Soc. **426,** 2957–2977 (2012) doi:10.1111/j.1365-2966.2012.21891.x

Herschel⋆ observations of extended atomic gas in the core of the Perseus cluster

Rupal Mittal,[1]† J. B. Raymond Oonk,[2] Gary J. Ferland,[3] Alastair C. Edge,[4] Christopher P. O'Dea,[5,6] Stefi A. Baum,[1,7] John T. Whelan,[8] Roderick M. Johnstone,[9] Francoise Combes,[10] Philippe Salomé,[10] Andy C. Fabian,[9] Grant R. Tremblay,[11] Megan Donahue[12] and Helen Russell[13]

[1]*Chester F. Carlson Center for Imaging Science, Rochester Institute of Technology, Rochester, NY 14623, USA*
[2]*Netherlands Institute for Radio Astronomy, Postbus 2, 7990 AA Dwingeloo, the Netherlands*
[3]*Department of Physics, University of Kentucky, Lexington, KY 40506, USA*
[4]*Institute for Computational Cosmology, Department of Physics, Durham University, Durham DH1 3LE*
[5]*Department of Physics, Rochester Institute of Technology, Rochester, NY 14623, USA*
[6]*Harvard–Smithsonian Center for Astrophysics, 60 Garden St., Cambridge, MA 02138, USA*
[7]*Radcliffe Institute for Advanced Study, 10 Garden St., Cambridge, MA 02138, USA*
[8]*School of Mathematical Sciences and Center for Computational Relativity & Gravitation, Rochester Institute of Technology, Rochester, NY 14623, USA*
[9]*Institute of Astronomy, Madingley Road, Cambridge CB3 0HA*
[10]*Observatoire de Paris, LERMA, CNRS, 61 Av. de l'Observatoire, 75014 Paris, France*
[11]*European Southern Observatory, Karl-Schwarzschild-Str. 2, 85748 Garching bei München, Germany*
[12]*Physics and Astronomy Department, Michigan State University, East Lansing, MI 48824, USA*
[13]*Department of Physics & Astronomy, University of Waterloo, N2L 3G1, Canada*

Accepted 2012 August 8. Received 2012 August 7; in original form 2012 June 18

ABSTRACT

We present *Herschel* observations of the core of the Perseus cluster of galaxies. Especially intriguing is the network of filaments that surround the brightest cluster galaxy, NGC 1275, previously imaged extensively in Hα and CO. In this work, we report detections of far-infrared (FIR) lines, in particular, [C II] 158, [O I] 63, [N II] 122, [O IB] 145 and [O III] 88 μm, with *Herschel*. All lines are spatially extended, except [O III], with the [C II] line emission extending up to 25 kpc from the core. [C II] emission is found to be co-spatial with Hα and CO. Furthermore, [C II] shows a similar velocity distribution to CO, which has been shown in previous studies to display a close association with the Hα kinematics. The spatial and kinematical correlation among [C II], Hα and CO gives us confidence to model the different components of the gas with a common heating model.

With the help of FIR continuum *Herschel* measurements, together with a suite of coeval radio, sub-millimetre and IR data from other observatories, we performed a spectral energy distribution fitting of NGC 1275 using a model that contains contributions from dust emission as well as synchrotron active galactic nucleus emission. This has allowed us to accurately estimate the dust parameters. The data indicate a low dust emissivity index, $\beta \approx 1$, a total dust mass close to $10^7\,M_\odot$, a cold dust component with temperature 38 ± 2 K and a warm dust component with temperature 116 ± 9 K. The FIR-derived star formation rate is $24 \pm 1\,M_\odot\,yr^{-1}$, which is in agreement with the far-ultraviolet-derived star formation rate in the core, determined after applying corrections for both Galactic and internal reddening. The total IR luminosity in the range 8–1000 μm is inferred to be $1.5 \times 10^{11}\,L_\odot$, making NGC 1275 a luminous IR galaxy.

⋆*Herschel* is an ESA space observatory with science instruments provided by European-led Principal Investigator consortia and with important participation from NASA.

†E-mail: rmittal@astro.rit.edu

We investigated in detail the source of the *Herschel* FIR and Hα emissions emerging from a core region 4 kpc in radius. Based on simulations conducted using the radiative transfer code, CLOUDY, a heating model comprising old and young stellar populations is sufficient to explain these observations. The optical line ratios indicate that there may be a need for a second heating component. However, stellar photoionization seems to be the dominant mechanism.

We have also detected [C II] in three well-studied regions of the filaments. *Herschel*, with its superior sensitivity to FIR emission, can detect far colder atomic gas than previous studies. We find an [O I]/[C II] ratio about 1 dex smaller than predicted by the otherwise functional Ferland (2009) model. That study considered optically thin emission from a small cell of gas and by design did not consider the effects of reasonable column densities. The line ratio suggests that the lines are optically thick, as is typical of galactic photodissociation regions, and implies that there is a large reservoir of cold atomic gas. This was not included in previous inventories of the filament mass and may represent a significant component.

Key words: dust, extinction – photodissociation region (PDR) – galaxies: clusters: individual: NGC 1275 – galaxies: clusters: intracluster medium – galaxies: ISM – galaxies: kinematics and dynamics.

1 INTRODUCTION

The Perseus cluster of galaxies is preeminent among the class of cool-core (CC) galaxy clusters (those with gas cooling times shorter than the Hubble time). This is in large part due to its close proximity ($z = 0.017\,56$), allowing detailed studies to be conducted in varying astrophysical contexts. It is the X-ray brightest galaxy cluster and has a strongly peaked surface-brightness profile. The intracluster gas in the inner few tens of kpc has a very short radiative cooling time (200–300 Myr). In the absence of heating, the expected X-ray mass deposition rate is several $100\,M_\odot\,yr^{-1}$. *FUSE* observations, on the other hand, suggest an actual cooling rate of $\sim 30\,M_\odot\,yr^{-1}$ (Bregman et al. 2006), and *XMM–Newton* RGS observations suggest an even lower residual cooling rate of $20\,M_\odot\,yr^{-1}$ (Fabian et al. 2006 and references therein).

Perseus is the prototype of cluster radio 'mini-haloes' (e.g. Pedlar et al. 1990; Gitti, Brunetti & Setti 2002). The brightest cluster galaxy (BCG) of Perseus (a giant cD galaxy), NGC 1275, is host to a powerful radio source, 3C 84. It has a Seyfert-like spectrum and a bolometric radio core-luminosity of the order of $10^{43}\,erg\,s^{-1}$ (e.g Vermeulen, Readhead & Backer 1994). 3C 84 is inferred to undergo episodic bursts of activity, blowing out jets of plasma which interact with the intracluster medium (ICM). *Chandra* X-ray images when compared with radio emission at different wavelengths (e.g. Böhringer et al. 1993; Fabian et al. 2000, 2006; Sanders, Fabian & Dunn 2005; Sanders & Fabian 2007) reveal the extent to which the central radio source has caused havoc in the ICM in the form of bubbles of various kinds (inner, outer, ghost), sound waves and shocks. On VLBI/VLBA (milliarcsec) scales, the radio morphology consists of a bright southern jet (e.g. Vermeulen et al. 1994; Taylor et al. 2006) believed to be pointed towards the observer and a dim northern counter-jet pointed away. The radio source shows a clear double-lobed morphology on smaller scales (∼80 arcsec) that extends into a more amorphous one on larger scales (∼170 arcsec).

One of the most intriguing aspects of Perseus is the spectacular network of ionized (Hα) and molecular (CO and H_2) gas filaments well beyond the optical stellar emission of the BCG. A significant number of BCGs in CC clusters show similarly extended filamentary structures, such as NGC 4696 (Centaurus), Abell 1795 and Hydra-A (Johnstone, Fabian & Nulsen 1987; Heckman et al. 1989; Sparks, Macchetto & Golombek 1989; Crawford et al. 1999; McDonald et al. 2010). The source of excitation of the filaments is currently one of the most pertinent issues in our understanding of CC galaxy clusters. In the case of NGC 1275, the filaments extend as far as ∼50 kpc out from the cluster-centric active galactic nucleus (AGN), with the mean surface brightness declining much slower than the inverse-square law. Photoionization from a central AGN thus seems unlikely. Similarly, ionizing radiation from hot stars, such as O and B type, has been ruled out based on anomalous emission lines in the spectra of the filaments (Johnstone & Fabian 1988; Johnstone et al. 2007; Ferland et al. 2008). Motivated by the observations of strong molecular hydrogen lines in NGC 4696 and NGC 1275, Ferland et al. (2009) showed that non-radiative heating, such as collisional heating from ionizing particles, can produce the observed emission. The importance of collisional excitation by energetic (ionizing) particles was suggested more than two decades ago by Johnstone & Fabian (1988). Candidate sources for these particles are either cosmic rays or the thermal electrons of the X-ray emitting ICM. Motivated by the spatial correspondence between the brightest low-energy X-rays and the Hα filaments, Fabian et al. (2011) considered the penetration of cold filaments by the surrounding hot X-ray gas through reconnection diffusion. More recently, Sparks et al. (2012) reported a detection with the *Hubble Space Telescope* (*HST*) Advance Camera for Survey (ACS) camera and also the Cosmic Origins Spectrograph (COS) of the [C IV]λ1549 line emission spatially coincident with the Hα line emission in M87 in Virgo. The [C IV]λ1549 line emission is indicative of gas at $\sim 10^5$ K. They suggested the origin of this line emission as being due to thermal conduction, i.e. the transport of energy by hot electrons from the hot ICM to the cold filament gas.

Various independent studies have provided strong evidence of the presence of dust in CC BCGs. These include dust continuum observations (e.g. Edge et al. 1999; Chapman et al. 2002; Egami et al. 2006; O'Dea et al. 2008; Rawle et al. 2012) and *HST* observations of BCGs with dust absorption features in them (e.g. McNamara et al. 1996; Pinkney et al. 1996; Laine et al. 2003; Oonk et al. 2011). Furthermore, observations of H_2 and CO molecular gas (e.g. Donahue et al. 2000; Edge 2001; Edge et al. 2002; Salomé et al. 2006) suggest that there is a substantial amount of dust present which provides shielding. In Mittal et al. (2011), we demonstrated

the need for an overabundance of dust (low gas-to-dust mass ratio) and metallicity to explain measurements in NGC 4696. In most of the cases, the gas-to-dust mass ratios are consistent with Galactic values (Sparks et al. 1989; Edge 2001); however, there is clearly an overabundance of dust in the filaments relative to the surrounding hot gas. The origin of the dust in the filaments is not yet clear. More recently, Voit & Donahue (2011) have suggested that the main source of dust in BCGs of CC clusters may be the stars of the central galaxy themselves. Thus, a stellar origin is plausible although in the case of NGC 1275 that seems unlikely given that the filaments exist out to a large radius from the galaxy core. Even though the sputtering time-scale for dust grains is short compared to the gas cooling time, optical observations have revealed magnificent dust lanes in some objects, which in many cases correlate spatially with the Hα filaments (Sparks et al. 1989; Donahue & Voit 1993; Crawford et al. 2005). Fabian (1994) and Voit & Donahue (1995) have proposed that gas-phase reactions create dust in the cold clouds that cool out of the ICM, which can then lead to an increase in dust through accretion on to existing grains. In contrast, several studies argue (e.g. Sparks et al. 1989; Farage et al. 2010) that the ionized gas and dust filaments originate from the stripping of a dust-rich neighbouring galaxy which may be in the process of merging with the BCG. The origin of the molecular and ionized filaments mixed with dust is to date an open question.

In this paper, we present *Herschel* observations of the core of the Perseus cluster. The main goal of this work is to investigate the source of the various emissions originating from the filaments. Far-infrared (FIR) data from *Herschel* (Pilbratt et al. 2010) have proven to be useful diagnostics of the heating mechanisms that account for the filaments in CC clusters (e.g. Edge et al. 2010a,b; Pereira et al. 2010; Mittal et al. 2011; Rawle et al. 2012). This work is part of a *Herschel* Open Time Key Project (PI: Edge) aimed at understanding the origin of cold gas and dust in a representative sample of 11 BCGs. We describe the data used and the analysis in Section 2. We present some basic results in Section 3 and move on to discuss the heating mechanisms prevailing in the core of NGC 1275 in Section 4 and those prevailing in the filaments of NGC 1275 in Section 5. We finally give our conclusions in Section 6. We assume throughout this paper the Λ cold dark matter concordance Universe, with $H_0 = 71\,h_{71}$ km s^{-1} Mpc^{-1}, $\Omega_{\rm m} = 0.27$ and $\Omega_\Lambda = 0.73$. This translates into a physical scale of 1 arcsec = 0.352 kpc and a luminosity distance of 75.3 Mpc at the redshift of NGC 1275 ($z = 0.017\,56$). This distance is consistent with the independent distance inferred from the 2005 Type Ia supernova SN2005mz (Hicken et al. 2009). The right ascension and declination coordinates in figures are in J2000 equinox. Lastly, NGC 1275 comprises two systems – a low-velocity system (LVS) consisting of gas at 5200 km s^{-1} associated with the BCG and a high-velocity system (HVS) consisting of gas at 8200 km s^{-1} associated with a foreground galaxy north-west (NW) of the BCG. In this work, NGC 1275 refers to the LVS system only unless otherwise mentioned. For calculation of line velocities we assume the velocity of the LVS to be the systemic velocity.

2 DATA AND ANALYSIS

2.1 *Herschel* data

We used the Photodetector Array Camera and Spectrometer (PACS; Poglitsch et al. 2010) to observe the [C II] line at 157.74 μm and the [O I] line at 63.18 μm, the two primary coolants of the interstellar medium (ISM). The [C II] and [O I] fine-structure lines are very often the brightest emission lines in galaxy spectra. In addition, we observed [O IB] at 145.52 μm, [Si I] at 68.470 μm, [N II] at 121.90 μm and [O III] at 88.36 μm. The [O I] and [C II] lines were observed in the raster-mapping mode, consisting of five raster lines and five points per line with a line step of 23.5 arcsec, whereas the rest of the lines were observed in a single-pointing mode. The observational parameters are summarized in Table 1. The line observations were conducted in the line-spectroscopy mode using the chopping and nodding technique (using a chopper throw of 6 arcmin) to subtract the telescope background, the sky background and the dark current.

The PACS photometric observations were made in large-scan mapping mode at a speed of 20 arcsec s^{-1} at blue-short (BS; 70 μm), blue-long (BL; 100 μm) and red (R; 160 μm) wavelengths (PI: E. Sturm; ObsIDs: 1342204217, 1342204218, 1342216022 and 1342216023). The scans consisted of 18 scan line legs of 4 arcmin length and of a cross-scan step of 15 arcsec. The 'scan' and orthogonal 'cross-scan' observations were individually calibrated before being combined into a single map of 9 arcmin × 9 arcmin. The PACS photometer has a resolution of 5.2, 7.7 and 12 arcsec at 70, 100 and 160 μm, respectively. The PACS photometer performs observations at BS and BL simultaneously with the *R* band, so we have two sets of scans in the *R* band. The photometric observations made with the Spectral and Photometric Imaging Receiver (SPIRE; Griffin et al. 2010) were also performed in the large-scan mapping mode and the data were recorded simultaneously at 250, 350 and 500 μm (PI: E. Sturm; ObsID: 1342203614). The SPIRE photometer has a resolution of about 18, 25 and 36 arcsec at these wavelengths, respectively.

The basic calibration of the data (spectral and photometric) was done using the *Herschel* Interactive Processing Environment (HIPE; Ott 2010) version 7.0 CIB 1931. For the PACS spectral data, the standard pipeline routines described in the PACS data reduction guideline were adopted to process the spectral data from their raw to a fully calibrated level. HIPE 7.0.1931 contains PACS calibration files that provide the response calibration based on in-orbit measurements. Hence, no ground-to-flight correction factors had to be applied. The PACS cubes were rebinned in wavelength using the Nyquist–Shannon sampling, corresponding to oversample = 2 and

Table 1. *Herschel* PACS spectroscopy observational log of NGC 1275 at a redshift of 0.017 56. All the lines were observed in the line-spectroscopy mode and on the same day: 2009 December 30.

Line	Peak rest λ (μm)	ObsID	Duration (s)	Bandwidth (μm)	Bandwidth (km s^{-1})	Spectral FWHM (μm)	Spectral FWHM (km s^{-1})	Spatial FWHM (arcsec)	Mode
O I	63.184	1342189962	9600	0.266	1250	0.017	79	9.4	5×5 raster, step size 23.5 arcsec
C II	157.741	1342214362	8600	1.499	2820	0.126	237	11.1	5×5 raster, step size 23.5 arcsec
N II	121.90	1342214363	3440	1.717	4180	0.116	280	10.6	Pointed
O IB	145.525	1342202581	3440	1.576	3215	0.123	250	9.7	Pointed
O III	88.356	1342214363	3680	0.495	1660	0.033	110	8.5	Pointed
Si I	68.473	1342202581	3840	0.218	945	0.014	62	8.3	Pointed

upsample = 1. The spatial full width at half-maximum (FWHM) varies from 8 arcsec for the [Si I] 68.47 μm line to 11 arcsec for the [C II] 157.74 μm line. The line fluxes were determined using the method described in Mittal et al. (2011). Briefly, the routine SPECPROJECT was used to obtain a final projection of the different pointings and nods on to the sky plane. These maps can be readily used to conduct 'aperture photometry' and measure fluxes. For PACS photometry, the data were reduced using the pipeline for the ScanMap observing mode, particularly designed to detect extended emission (>100 arcsec). The pipeline employs a second-level deglitching algorithm, which uses the redundancy in a pixel to flag outliers, so that bright sources are not erroneously flagged as glitches. For SPIRE photometry, the data were reduced using the pipeline for the LargeScanMap observing mode and the NAIVE map-maker.

2.2 Hα data

The Hα flux measurements were made using the continuum-subtracted data from Conselice, Gallagher & Wyse (2001). Based on comparison with our newer *HST* data (Fabian et al. 2008), the calibration of the WIYN data appears to overestimate the flux by a factor of about 3. The source of this discrepancy is yet not clear and is under thorough investigation (Johnstone et al., in preparation). To verify the calibration offset of the WIYN continuum-subtracted image, we calculated the total flux in the WIYN Hα image in counts per second and converted it into erg s^{-1} cm^{-2} using the conversion given in Conselice et al. (2001). We were only able to derive the total luminosity quoted in Conselice et al. (2001), and which is in good agreement with Heckman et al. (1989), after lowering the total flux by a factor of 3. Hence, we have scaled down the measured WIYN Hα fluxes by a factor of 3.

The *HST* broad-band filter F625W admits light from the [O I]λ6300, [N II]λ6583 and [S II]λ6731 doublets as well as Hα. The ratios of these lines to Hα are variable with position in the nebula. Such spectroscopic data are available for only a small fraction of the total area covered by the entire nebula. For the WIYN data the contamination is only from the [N II]λ6583 doublet. This is the main reason why we prefer to use the WIYN data.

Hatch et al. (2006) found a radial gradient in the ratio [N II]λ6583/Hα, which may be due to a spatially varying metallicity or excitation mechanism (see also Johnstone & Fabian 1988). They used the multi-object spectrograph instrument on *Gemini* and found that the [N II]λ6583/Hα ratio varies from 0.5 to 0.85 in the Horseshoe region. Assuming that the [N II]λ6583/Hα ratio does not change significantly with azimuthal angle, we subtracted the contribution of [N II]λ6583 from the measured Hα flux in the Horseshoe, south-west (SW) and Blue Loop knots, using an average ratio of [N II]λ6583/Hα = 0.65. The *Gemini* measurement close to the nucleus indicates an [N II]λ6583/Hα ratio close to unity; therefore, we halved the measured Hα flux in the core region. Similarly, we also corrected for the [N II]λ6548 line, usually a third in intensity of the [N II]λ6583 line (Hatch et al. 2006).

Due to the uncertainties in the [N II]λ6583/Hα ratio and the calibration of the WIYN data, we caution the reader concerning the absolute values of the Hα fluxes. However, the relative values of Hα flux between spatial positions should be accurate. The Hα amplitude plays a role in Section 4, where the *Herschel* and Hα measurements are used as constraints to determine the heating mechanisms giving rise to the various emissions. Fortunately, there are enough FIR-derived constraints that the best-fitting model parameters do not rely solely on the Hα flux measurement.

2.3 Dust extinction

Submillimetre Common-User Bolometer Array (SCUBA) observations of NGC 1275 have been used to infer the presence of a large amount of dust (6×10^7 $M_\odot$) present (Irwin, Stil & Bridges 2001). The source of dust is not yet clear and understanding it is one of the goals of this study. However, dust also presents a hindrance due to the extinction it causes at optical and higher frequencies. In this work, both the Galactic and internal extinction corrections, such as for Hα (Section 2.2) and far-ultraviolet (FUV) measurements (Section 4.3), were calculated with the help of the mean extinction laws given in Cardelli, Clayton & Mathis (1989). We assumed the Galactic extinction law, $R_V = 3.1$, and an $E(B-V)$ value of 0.163 from the NASA/IPAC Extragalactic Database (NED[1]). Internal extinction was calculated using the observed Balmer decrements, which were compared to the case-B value of Hα/Hβ = 2.86. For the filaments located far out from the core, an internal extinction of $E(B-V) = 0.38$ was estimated based on the Galactic-extinction corrected Balmer decrement, Hα/Hβ = 4.2, as measured in the Horseshoe knot (Ferland et al. 2009). For the core, a similar internal extinction was estimated, $E(B-V) = 0.37$, based on the Galactic-extinction corrected Balmer decrement, Hα/Hβ = 4.08, as measured 18 arcsec SW of the nucleus by Kent & Sargent (1979). Note that Kent & Sargent (1979) obtain an internal reddening of $E(B-V) = 0.43$ assuming a Galactic extinction of $E(B-V) = 0.1$. We obtain a lower internal reddening due to the higher Galactic extinction adopted.

The correction factor for the internal reddening is model dependent. If the Hα and Hβ emissions are produced by another mechanism than case-B recombination, then the Balmer decrement will be different from the expected value of 2.86. For example, if particle heating is responsible for the Hα and Hβ emissions, then the intrinsic Balmer decrement will be higher and consequently the deduced internal reddening lower.

3 RESULTS

Of the six lines observed, we detected all except [Si I] at 68.47 μm. Even though only [C II] and [O I] observations were designed to detect extended emission, all the detected lines except [O III] are spatially extended. The integrated line profiles are shown in Fig. 1 and their relative spatial extensions in Fig. 2, where the pixel threshold has been set to SNR > 2. The SNR corresponds to the ratio of the line peak to the standard deviation of the data about the fitted model. Listed in Table 2 are the integrated line properties.

The [C II] line is detected over a spatial region of extent 140 arcsec (50 kpc). Shown in the left-hand panel of Fig. 3 is an Hα+[N II]λλ6583, 6548 image displaying the ionized gas filaments taken with the WIYN 3.5 m telescope (Conselice et al. 2001). Shown in the right-hand panel of Fig. 3 is the FIR [C II] emission with the pixel detection threshold set to SNR >1. The middle panel displays the Hα emission smoothed to match the resolution of the [C II] line using the CIAO tool 'ACONVOLVE' and the PYRAF tool 'BLKAVG', with the [C II] line contours overlaid (in red). The [C II] emission traces the Hα emission very well despite a much lower resolution. Both [C II] and Hα reveal a central elongation, about 20 kpc in total extent, with an east–west alignment. This elongation is clearly visible also in the recent narrow-band imaging of a ro-vibrational transition line of molecular hydrogen (H_2; Lim et al. 2012), which shows very good overall morphological resemblance

[1] http://nedwww.ipac.caltech.edu

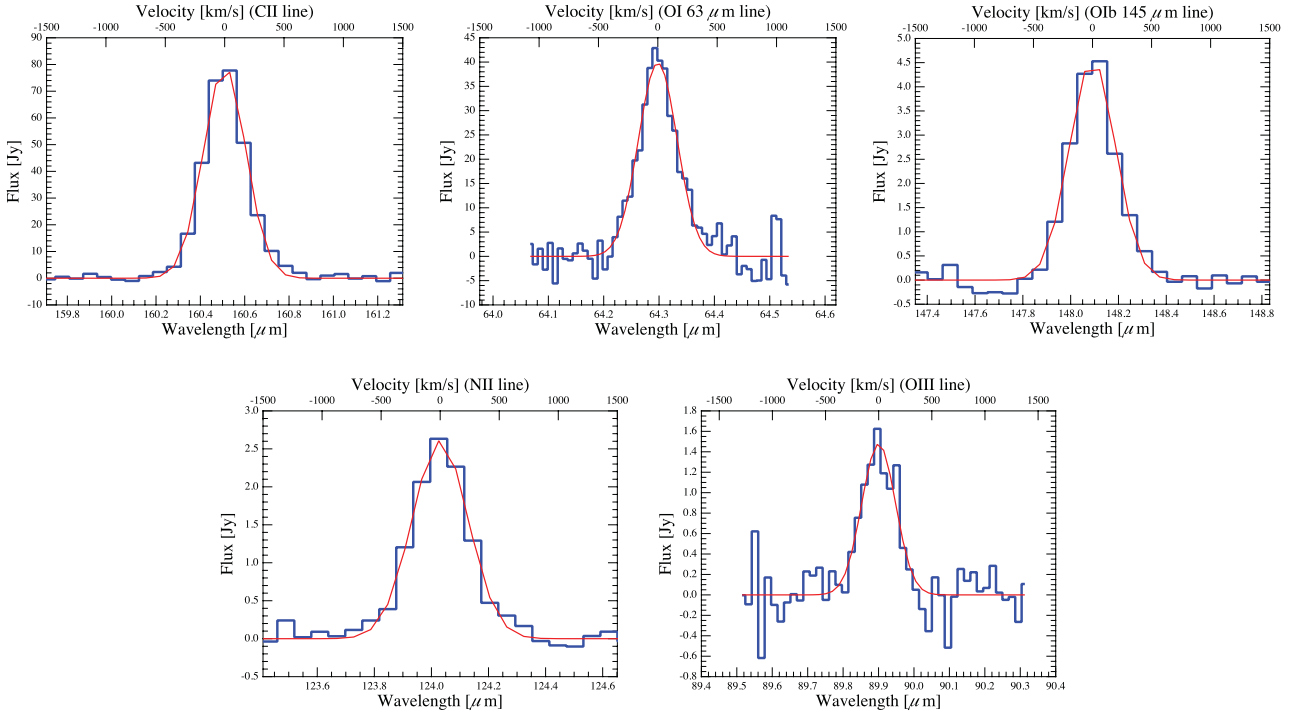

Figure 1. The forbidden FIR line detections in the centre of NGC 1275 made with the *Herschel* PACS instrument. The lines are spatially integrated. Top row: [C II] 157.74 μm (left), [O I] 63.18 μm (middle) and [O IB] 145.52 μm (right). Bottom row: [N II] 121.90 μm (left) and [O III] 88.36 μm (right).

with Hα emission. In Mittal et al. (2011), we showed a close spatial and kinematical correspondence between different emissions, such as Hα and [C II], in NGC 4696, the BCG of the Centaurus cluster. NGC 1275 shows a similarly tight correlation, both spatial and kinematical, between [C II], Hα and CO (Section 3.1), suggesting a common heating process of the gas.

There are three well-studied regions in the Hα filaments, seen also in the [C II] map, which we briefly describe below. (1) The Horseshoe is a filament to the NW of the centre of BCG (Conselice et al. 2001). The filament of gas appears to originate in the core of the galaxy, rising a projected distance of 26 kpc through the ICM before looping around towards the centre again. (2) The SW knots, at a projected distance of ∼23 kpc from the centre of the BCG, are a part of the southern filaments. (3) The knots in the south-east (SE) filament, also known as the 'Blue Loop', are at a projected distance of ∼16 kpc. The loop is so called due to the blue optical colour of the knots this region, indicating that these are star-forming sites. Canning et al. (2010) studied this region in detail and found a star formation rate (SFR) of $\sim 20\,M_{\odot}\,yr^{-1}$. We refer to the knots as the 'Blue Loop' knots from now on. All three regions have been studied in detail previously at several wavelengths (Conselice et al. 2001; Fabian et al. 2003, 2008; Hatch et al. 2005, 2006; Salomé et al. 2006, 2008, 2011; Johnstone et al. 2007; Ferland et al. 2009; Canning et al. 2010).

The three regions are marked in Fig. 3. We extracted the [C II] line spectra from them and the core region (see below). The spectra are shown in Fig. 4. The Horseshoe region is weaker in [C II] emission than the SW and Blue Loop knots. This is consistent with the study of Salomé et al. (2011), where they find that this region has weaker CO emission in comparison with other filaments. There is no detection of [O I] in any of the three regions of the filaments. The line strengths and ratios in these regions and the core provide strong constraints for studying the excitation mechanism(s) in different parts of the BCG. This is followed up in detail in Section 5.

Brauher, Dale & Helou (2008) report a flux of $(2.5 \pm 0.2) \times 10^{-15}$ W m^{-2} for [O I] and $(1.2 \pm 0.1) \times 10^{-15}$ W m^{-2} for [C II], based on observations with the long wavelength spectrometer (LWS) on the *Infrared Space Observatory* (*ISO*). While the [O I] flux measurement of $(2.53 \pm 0.07) \times 10^{-15}$ W m^{-2} obtained in this study compares well with the *ISO* measurement, our [C II] flux of $(2.21 \pm 0.03) \times 10^{-15}$ W m^{-2} is higher by a factor of 2. The reason for this discrepancy is that Brauher et al. (2008) obtain the [C II] flux based on the assumption that NGC 1275 is a point source. The FWHM of the LWS is 75 arcsec. However, [C II] emission clearly extends beyond the FWHM of the LWS (∼140 arcsec in diameter). For this reason, we believe that Brauher et al. (2008) underestimate the line flux in [C II] by about a factor of 2. As a rough check of this hypothesis, we convolved our [C II] map with a Gaussian with an FWHM of 75 arcsec and obtained a flux of 0.97×10^{-15} W m^{-2} within a 75 arcsec aperture diameter. Despite the fact that this test uses a simple Gaussian rather than the true *ISO* LWS beam profile, the reduction of measured flux is consistent with the result of Brauher et al. (2008).

3.1 Kinematics

Fig. 5, the [C II] velocity distribution, shows the full extent of the complex kinematical structure of the filaments in NGC 1275. The colour scheme is such that the red shaded regions represent redshifted gas (with positive velocities with respect to the systemic velocity of the BCG), whereas green and blue shaded regions represent blueshifted gas (with negative velocities with respect to the systemic velocity of the BCG). The velocity pattern is likely to be the combination of inflowing and outflowing gas, along with projection and small-scale rotation effects (see below).

The dashed circle at the centre marks the 'core' region (see Table 7), which shows a gradient in the [C II] line velocity. Wilman, Edge & Johnstone (2005) conducted near-IR (NIR) spectroscopy of

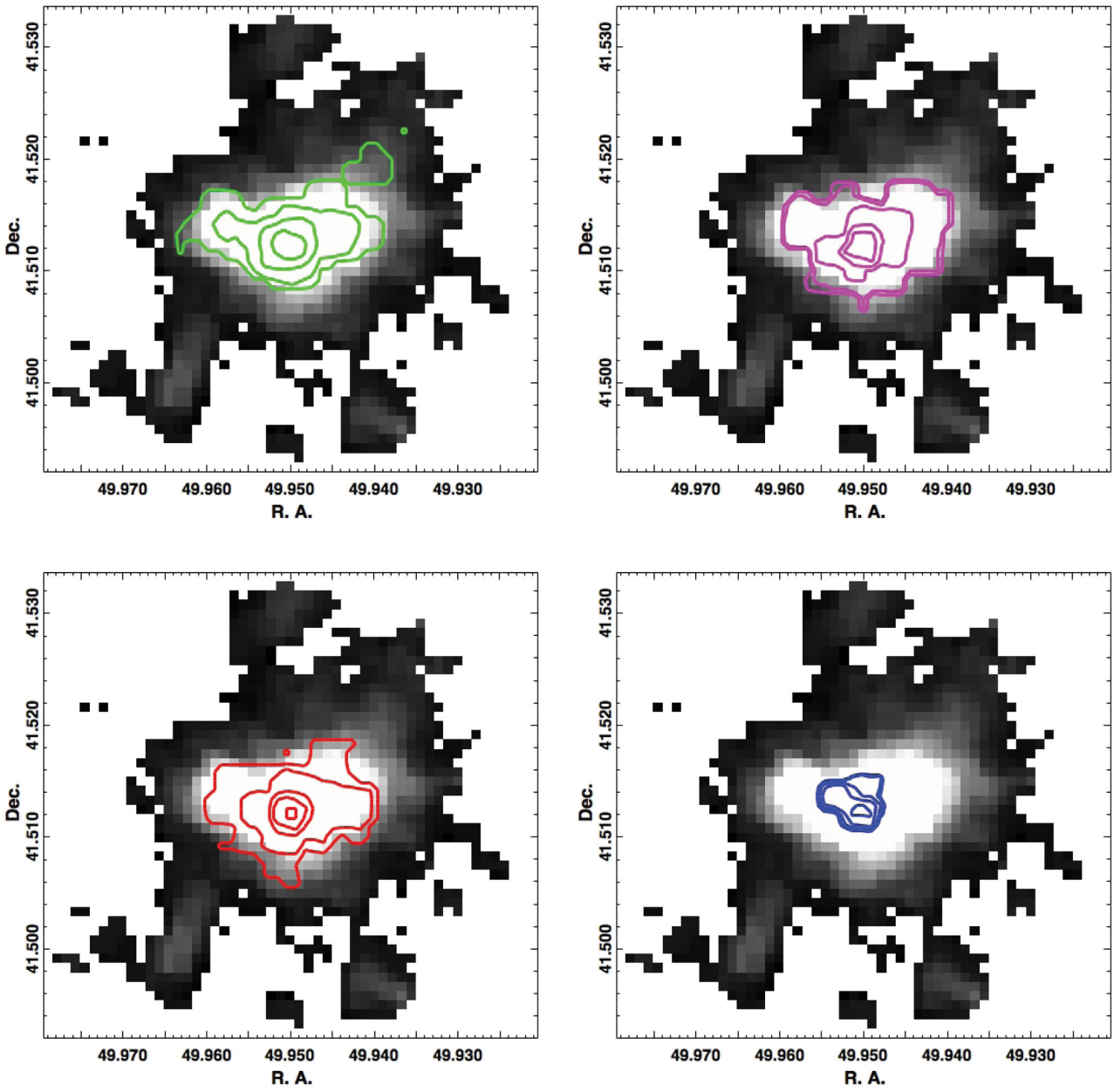

Figure 2. A comparison of the *Herschel* emission lines. Overlaid on the [C II] image (grey-scale) are (starting from the upper-left corner and going clockwise) the [O I] contours (green), [N II] contours (magenta), [O IB] contours (red) and [O III] contours (blue). All emission lines have a pixel detection threshold of SNR >2.

Table 2. Integrated line properties. Also given is the 3σ upper limit for the [Si I] line flux. The spatial extents are based on visual inspection.

Line	λ (μm)	Offset (km s^{-1})		FWHM (km s^{-1})		Line flux	Spatial extent (Radius)	
		z_{bcg}	z_{cl}	Obs.	Intrinsic	(10^{-18} W m^{-2})	(arcsec)	(kpc)
[O I]	64.298 ± 0.002	39 ± 9	−61 ± 9	383 ± 20	375 ± 20	2525.8 ± 73.7	34	12
[C II]	160.510 ± 0.002	−0.6 ± 4	−100 ± 4	419 ± 9	347 ± 11	2205.3 ± 26.5	71	25
[N II]	124.031 ± 0.004	−24 ± 10	−124 ± 10	558 ± 22	482 ± 25	125.0 ± 2.8	28	10
[O IB]	148.091 ± 0.003	32 ± 7	−68 ± 7	458 ± 17	384 ± 20	150.5 ± 3.1	29	10
[O III]	89.900 ± 0.005	−37 ± 17	137 ± 17	375 ± 42	358 ± 44	65.6 ± 4.1	<9.4	<3.3
[Si I]	–	–	–	–	–	<3.6	–	–

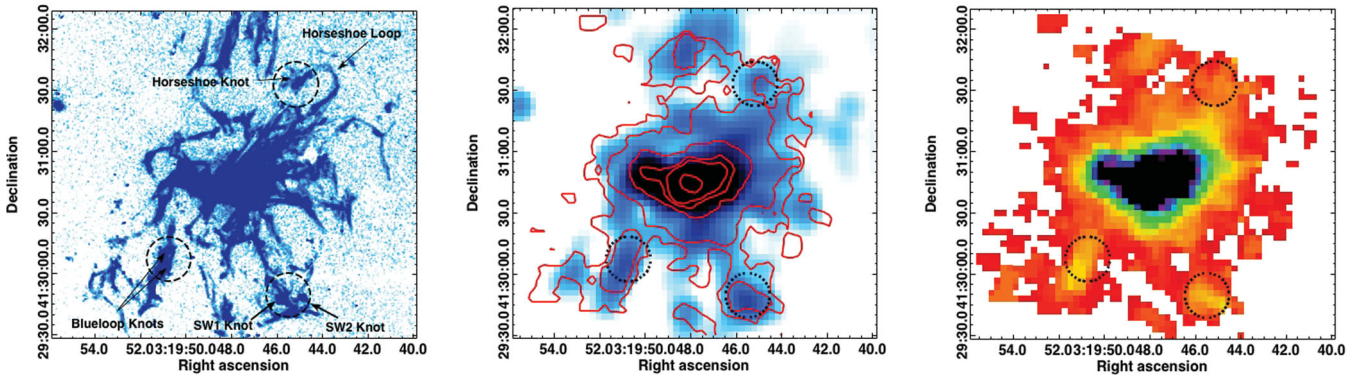

Figure 3. Left: the continuum-subtracted WIYN Hα line emission with a spatial resolution of 0.6 to 0.8 arcsec (Conselice et al. 2001). Middle: the Hα image smoothed to the resolution of [C II], with the [C II] line contours overlaid in red. Right: the *Herschel* [C II] line emission with a spatial resolution of 11 arcsec (this work). The optical Hα emission and IR [C II] emission show a remarkably similar distribution. Marked are the Horseshoe knot in the NW 20 kpc from the BCG, the SW1/SW2 knots in the SW 21 kpc from the BCG and the Blue Loop knots in the SE 16 kpc from the BCG.

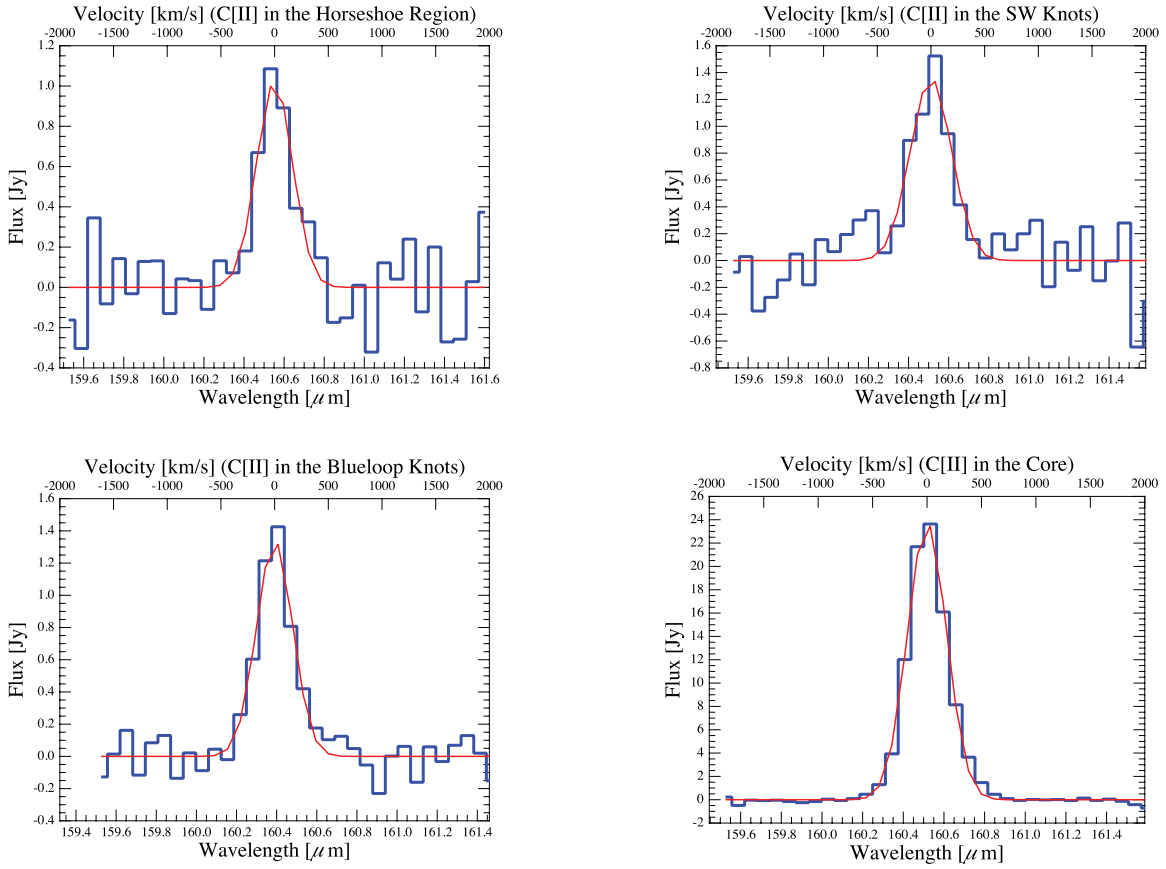

Figure 4. The [C II] emission from the Horseshoe knot in the NW (upper-left panel), the SW1/SW2 knots in the SW (upper-right panel) and the Blue Loop knots in the SE (lower-left panel). These apertures are marked in Fig. 3. We also show the [C II] spectrum for the core region (lower-right panel), marked in the upper-left panel of Fig. 5.

the central region in NGC 1275 with the UIST IFU instrument on the United Kingdom Infrared Telescope. They detected ro-vibrational H_2 emission originating from a region ~50 pc from the nucleus, with the results indicating a strong velocity gradient in the peak position of the H_2 line. The measured rotation curve in the central IFU slit placed east–west along the nucleus shows a velocity change from 150 km s^{-1} east of the nucleus to −100 km s^{-1} west of the nucleus. From the sharp decrease in the magnitude of the velocity on either side of the nucleus, they concluded that the molecular gas is distributed in a disc-like structure with the rotation axis oriented north–south. This is also consistent with the double-horn structure seen in the CO(2–1) spectrum extracted from the same core region (Salomé et al. 2011), which may be interpreted as indirect evidence for a central rotating disc. The resolution of the [C II] data is not good enough to resolve any rotational structure over the scales observed by Wilman et al. (2005). The smallest structure in [C II] that can be resolved is about 4 kpc. Similarly, the spectral resolution of the [C II] data (230 km s^{-1}) is much poorer than that of the CO(2–1) line

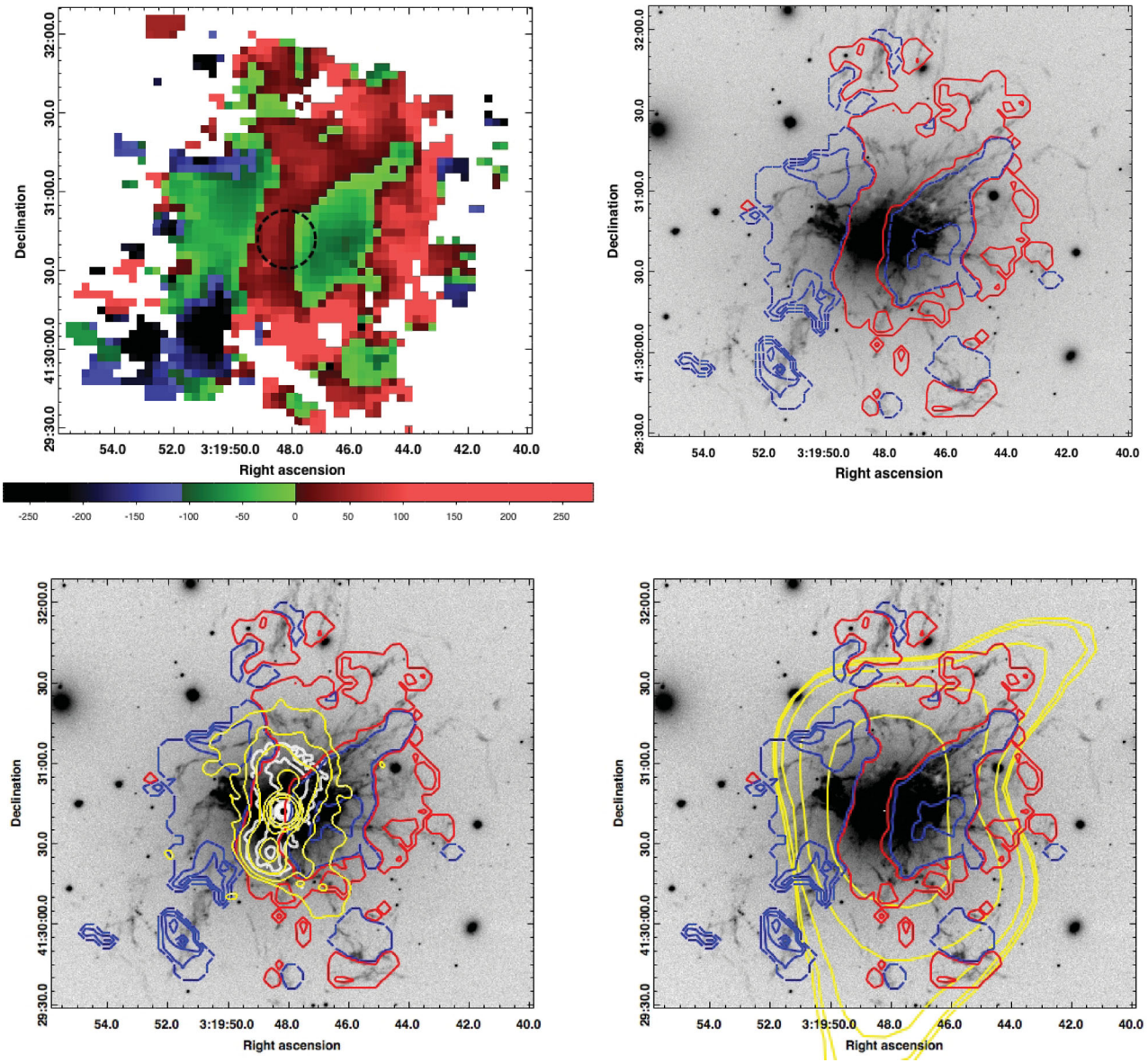

Figure 5. Upper-left: the detailed velocity distribution of the [C II] gas. The colour bar represents the velocities in km s^{-1}. The dashed circle represents gas compatible with rotation. Upper-right: the velocity contours superimposed on the Hα image. The dashed blue contours correspond to the blueshifted (negative) velocities and the solid red contours correspond to the redshifted (positive) velocities. Bottom-left: 1.4 GHz radio contours at two different resolutions, 2 arcsec (white) and 5 arcsec (yellow), overlaid on the Hα image. Bottom-right: 74 MHz radio contours at 25 arcsec resolution (yellow) overlaid on the Hα image.

observed with the IRAM 30 m telescope on Pico Veleta (40 km s^{-1}). From Fig. 5, the rotational pattern claimed by Wilman et al. (2005) and Salomé et al. (2011) is not surprising. However, it is difficult to say whether the double-horn feature is due to small-scale disc-like rotation or large-scale flows. If there is a rotating disc present in the centre, it involves a relatively small gas disc of ∼5 kpc radius. The majority of the gas distribution sampled by [C II] does not show any regular rotation.

Also interesting is the redshifted ridge of gas passing through the centre of the BCG with a north–south extension. The CO velocity measurements made by Salomé et al. (2011) in regions 4 and 21 marked in fig. 1 of their paper provide a confirmation of the presence of this redshifted gas (also see Lim, Ao & Dinh-V-Trung 2008). This wide vertical distribution of gas has a cylindrical symmetry and is suggestive of material being dragged upward and downward.

The upper-left panel of Fig. 5 shows that there is a negative velocity region on either side of the centre along the east–west direction. The east region extends all the way along to the south, where it merges with the Blue Loop knots. The blueshifted components on both sides of the major axis of the emission are also visible in the kinematics inferred from the CO spectra (Salomé et al. 2006). The CO flux and velocity distribution show a close association with the optical filaments seen in Hα (e.g. Salomé et al. 2006). In Fig. 6, we show the kinematics of the gas in the inner 90 arcsec × 90 arcsec in three phases – optical, FIR and millimetre – as represented by Hα [taken from Conselice et al. (2001)], [C II] and CO(2–1) [taken from Salomé et al. (2006)] line emissions. This plot shows a clear overlap in the redshifted gas, with absolute velocities greater than 5264 km s^{-1} (red symbols), along the ridge associated with all three line emissions. Similarly, there is an overlap in the blueshifted gas,

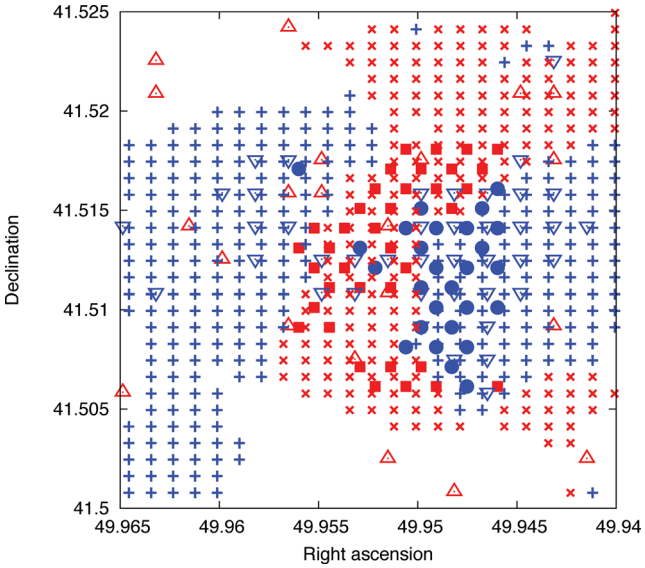

Figure 6. The kinematics of the three phases, optical, FIR and millimetre, represented by Hα, [C II] and CO(2–1) line emissions, respectively. Shown are the redshifted (red symbols) and blueshifted (blue symbols) velocities for the three phases. The [C II] velocities are shown as plus (blueshifted) and cross (redshifted) symbols, the Hα velocities are shown as filled circles (blueshifted) and squares (redshifted) and CO(2–1) velocities are shown as open down-triangles (blueshifted) and up-triangles (redshifted).

with absolute velocities less than 5264 km s^{-1} (blue symbols), west of the ridge. Especially remarkable is the curvature in the ridge seen in both Hα (red filled squares) and [C II] (red crosses). From this we conclude a kinematical correlation among [C II], Hα and CO emissions, which further reinforces the idea that different emissions have the same origin.

Radio observations of central radio sources often provide useful insights in understanding the kinematics of CC BCGs. Overlaid on the bottom panels of Fig. 5 are contours of the radio emission associated with 3C 84 at 1.4 GHz and 74 MHz. The bottom-left panel shows 1.4 GHz radio emission at two different resolutions – 2 arcsec (white contours; courtesy of Very Large Array/NRAO[2]) and 5 arcsec (yellow; kindly provided by Greg Taylor). The higher resolution contours reflect a north–south radio morphology, demonstrating a good alignment with the redshifted [C II] contours. The lower resolution contours reflect an inverted-S-shaped morphology, previously noted in several studies (e.g. Pedlar et al. 1990; Böhringer et al. 1993; Fabian et al. 2000). Although the southern jet shows a correlation with the [C II] emission, the tip of the northern jet does not. The 74 MHz contours (also kindly provided by Greg Taylor), shown in yellow in the bottom-right panel, indicate a reversal of the east–west component of the jet direction on both sides of the core, wherein the northern jet once again overlaps with the [C II] emission. Conselice et al. (2001) noted a similar alignment between the linear extension of the Hα filaments to the north and the low-brightness radio emission seen at low frequencies.

Several studies have presented scenarios wherein radio outbursts are responsible for the dredge-up of cold, metal-rich gas from the core in the direction of the buoyantly rising radio plasma (e.g. Revaz, Combes & Salomé 2008; Simionescu et al. 2008, 2010; Gitti et al. 2011; Tremblay et al. 2012a,b). Evidence for these scenarios is based on the X-ray-derived temperature and metallicity maps, which show a spatial correlation between radio emission and cool gas extending away from the core with a metal content higher than that of the ambient medium. The positive correlation between the radio emission and the redshifted ridge of [C II] gas in NGC 1275 is reminiscent of cold gas being dredged up by the radio lobes. On the other hand, this interpretation implies that both the radio jets (jet and counter-jet) are pointed away from the line of sight. On milliarcsec scale, the radio morphology comprises a one-sided jet, such that the southern jet is deemed to be approaching, and the northern jet (counter-jet) receding (e.g. Pedlar et al. 1990; Vermeulen et al. 1994; Dhawan, Kellermann & Romney 1998; Taylor et al. 2006). Both the radio jets reveal complex kinematics in the plane of the sky. The southern jet is initially elongated along position angle (PA) $\sim$235° (at $\sim$10 mas) but suddenly bends towards PA $\sim$ 160° (at $\sim$20 mas) and continues though a series of such bends, at approximately the same angles, out to about an arcminute (Pedlar et al. 1990; Dhawan et al. 1998). The northern jet exhibits a similar complex structure. On the kiloparsec scale, it is therefore possible that, similar to the kinks observed in the plane of the sky, the jets undergo bends along the line of sight, such that both the jets are receding. There are dredge-up interpretations offered for NGC 1275, suggesting that Hα gas is being dredged up by the radio source. Fabian et al. (2003) recognized two filaments in the NW, including the Horseshoe, bent on either side of the NW ghost bubble. They showed that the Hα emission associated with the Horseshoe is just behind the bubble and is likely dragged out by it. Similarly, Sanders et al. (2005) discovered a high-abundance ridge using *Chandra* observations, which they hypothesized is formed by material entrained by a fossil radio bubble.

Lastly, the [C II] velocity structure may be related to the disordered motion of gas clouds at larger radii that is not affected by the inner radio structure. Shown in Fig. 7 is the [C II] linewidth in km s^{-1}. An interesting feature of this map is that the linewidth peaks along the redshifted ridge where the line velocity flips from positive to negative on the eastern side of the galaxy. This is where the CO(3–2) HARP maps show double lines implying that there are multiple gas components along the line of sight (Edge et al., in preparation). However, the linewidths in this region may also be high due to the superposition of rapidly varying line-of-sight velocity elements.

3.2 Spatial variation of the [O I] to [C II] ratio

Here we briefly discuss the spatial variation of the [O I] to [C II] ratio and what may be inferred from it. The resolution of the [C II] line is slightly poorer than the [O I] line. For compatibility, we convolved the [O I] line map with a Gaussian such that the resulting FWHM is similar to that of the [C II] line. Fig. 8 is obtained by dividing the resulting smeared [O I] map by the [C II] map (the threshold for both [C II] and [O I] was set to SNR $>$ 2). This figure indicates that while [O I] is stronger than [C II] in the core, the opposite is true at larger radii, namely the [C II] line emission becomes stronger at radii larger than $\sim$4 kpc, which corresponds to the spatial resolution of [C II].

The relative strength of [O I] to [C II] is an indicator of gas density, such that a higher [O I]/[C II] ratio represents a higher density gas for the reasons described in Section 4.1. Hence, a higher [O I]/[C II] ratio in the centre implies a relatively denser gas in the cluster core, as expected.

[2] The National Radio Astronomy Observatory is a facility of the National Science Foundation operated under cooperative agreement by Associated Universities, Inc.

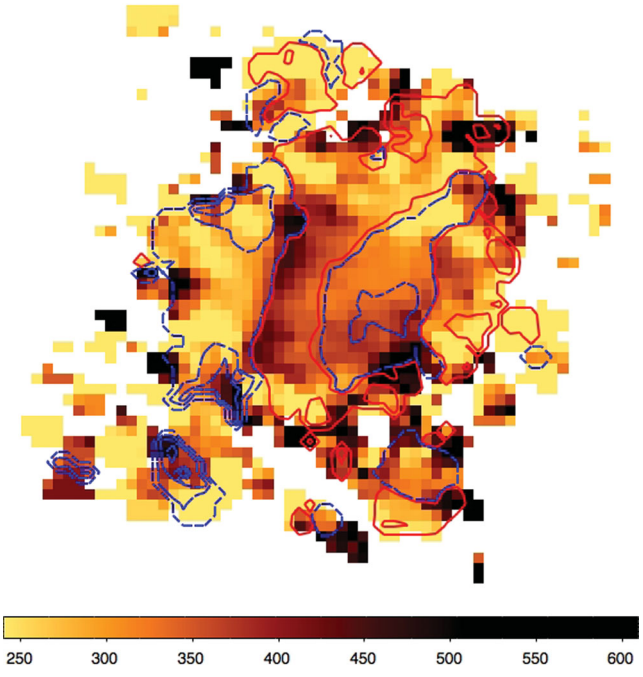

Figure 7. The [C II] linewidth in km s^{-1}. The dashed blue contours correspond to the blueshifted (negative) [C II] velocities and the solid red contours correspond to the redshifted (positive) [C II] velocities (same as the upper-right panel of Fig. 5).

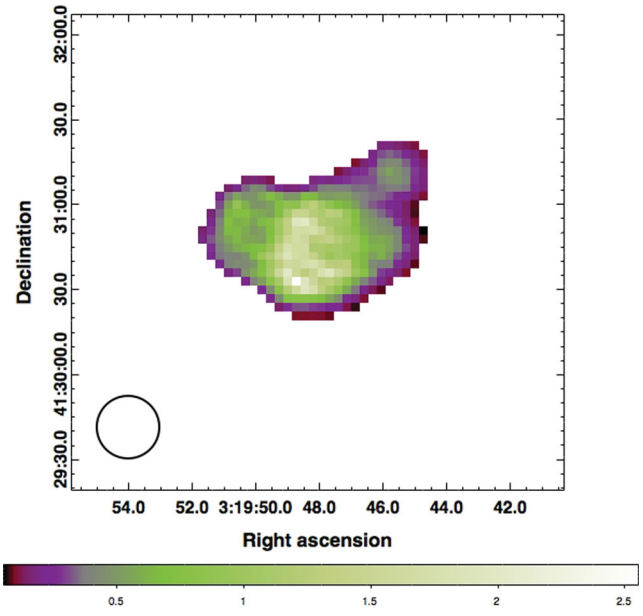

Figure 8. [O I] to [C II] ratio. [O I] has been convolved with a Gaussian such that the resulting FWHM equals that of the PSF of the PACS spectrometer at the wavelength of [C II]. The circle shown in the bottom-left corner represents the size of the FWHM. The ratio map shows that [O I] is stronger than [C II] in the core. The trend reverses at ∼4 kpc from the centre.

3.3 Dust SED

We detected emission at all three PACS wavelengths and all three SPIRE wavelengths. The PACS images are shown in Fig. 9. Dust emission can usually be modelled as a simple modified blackbody function; NGC 1275, though, poses a complication. This is because of the strong radio source at the centre of NGC 1275, with a large contribution in the sub-mm and FIR range (Irwin et al. 2001). The radio source, additionally, shows a large-amplitude variability on time-scales of decades (see Nagai et al. 2012 and references therein). Detailed monitoring at 3 mm has shown an increase in flux from 3.5 Jy in 2002 to 11 Jy in 2010 (Trippe et al. 2011).

In order to obtain accurate dust parameters, it is essential to estimate the fraction of the FIR flux originating from the synchrotron emission from 3C 84. In the following, we attempt to simultaneously fit the dust and AGN emissions. We list in Table 3 and show in Fig. 10 the various flux measurements (black filled diamonds) that were used to obtain an optimal model. While the dust contribution to the spectral energy distribution (SED) is constrained by the PACS (blue open diamond) and SPIRE (red filled triangles) data, the synchrotron contribution is constrained by radio and sub-millimetre (sub-mm) data. The two subsets of sub-mm flux densities clustered around 1 and 3 mm (yellow filled squares) correspond to the IRAM Plateau de Bure Interferometer (Trippe et al. 2011) observations. These measurements are from a monitoring programme and chosen so as to be closest in time (spanning days between 2010 August 21–29) to the SPIRE and PACS observations. The 5, 8 and 15 GHz radio measurements (purple diagonal-plus symbols) correspond to the observations made in 2010 with the 26 m telescope at the University of Michigan Radio Astronomy Observatory (UMRAO, courtesy of M. Aller and H. Aller). We used only the 15 GHz data point for the fitting since the spectrum turns over below this frequency, indicative of synchrotron self-absorption. The 50 and 25 μm measurements (green filled circles) correspond to the *IRAS* observations (Moshir et al. 1990). To obtain a robust estimate of the temperature and mass of the plausible second (warm) dust component, we also used the 20 and 30 μm continuum data (red open crossed-squares) determined from the *Spitzer* InfraRed Spectrograph (IRS) observations (Weedman et al. 2005). We did not fit 6, 10 and 15 μm data due to a possibly increasing contribution from a passively evolving population of stars at wavelengths $\lesssim$15 μm. The AGN synchrotron contribution to the total emission is expected to be small at wavelengths shorter than 70 μm, and so the variation in the flux density due to the different times of the *IRAS*/*Spitzer* observations from the rest of the fitted data can be neglected.

To model both the components – the dust emission and AGN synchrotron emission – we used the following fitting function:

$$S_\nu = S_{\mathrm{syn},\nu} + S_{\mathrm{dust},\nu}\ , \quad \text{where} \tag{1}$$

$$S_{\mathrm{syn},\nu} = \begin{cases} S_0 \left(\frac{\nu}{\nu_0}\right)^{\alpha_1} & \text{if } \nu < \nu_{\mathrm{break}} \\ S_0 \left(\frac{\nu_{\mathrm{break}}}{\nu_0}\right)^{\alpha_1-\alpha_2} \left(\frac{\nu}{\nu_0}\right)^{\alpha_2} & \text{if } \nu \geq \nu_{\mathrm{break}} \end{cases}, \tag{2}$$

$$S_{\mathrm{dust},\nu} = \frac{\Omega}{(1+z)^3}\ [B_\nu(T_\mathrm{d}) - B_\nu(T_\mathrm{cmb})]\ (1 - \mathrm{e}^{-\tau_\nu(M_\mathrm{d})}); \tag{3}$$

equation (2) quantifies the synchrotron emission assumed to have a broken power-law form. S_0 denotes the normalization at ν_0 = 100 GHz (3 mm), α_1 and α_2 and the (negative) power-law indices on either side of the power-law break frequency, ν_{break}, respectively (α_1 representing the power law at radio frequencies and α_2 representing the power law at sub-mm/FIR frequencies). We find that for NGC 1275 it is not necessary to modify the synchrotron emission with an exponential term like Privon et al. (2012) did to model the spectrum of Cygnus A. The need for including an exponential term in the case of Cygnus A arises from the lack of synchrotron emission beyond the sub-mm regime. NGC 1275, on the other hand, shows evidence of an AGN contribution all the way out to sub-mm and,

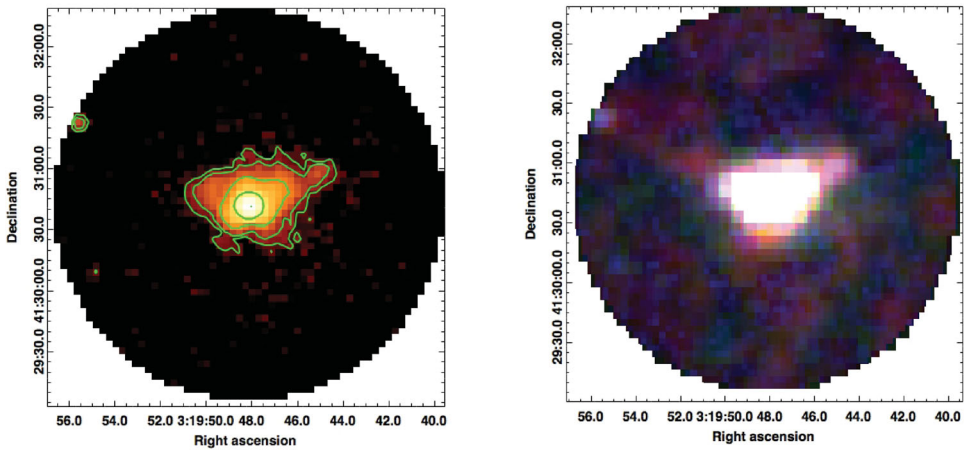

Figure 9. Dust emission. Left: PACS 100 μm image at a resolution of 7 arcsec showing the extended dust features. Right: PACS images convolved with a Gaussian to yield an FWHM of 12 arcsec. The 70 μm image is shown in blue, the 100 μm image in green and the 160 μm image in red.

Table 3. A compilation of the fitted radio, sub-mm and IR flux densities for NGC 1275. The columns are (1) wavelength, (2) instrument, (3) year of the observation, (4) aperture (available only for this work) and (5) the measured flux density. Note that the measurements correspond to the total flux densities for the given instrument.

λ (μm)	Instrument	Year	Aperture (arcsec)	Flux (mJy)
20	*Spitzer* IRS[d]	2004	–	2410 ± 241
25	*IRAS*[c]	1983	–	3539 ± 176
30	*Spitzer* IRS[d]	2004	–	3820 ± 382
60	*IRAS*[c]	1983	–	7146 ± 286
70	PACS *Herschel*[a]	2011	55	7405 ± 741
100	PACS *Herschel*[a]	2010	55	8541 ± 854
160	PACS *Herschel*[a]	2010	55	6979 ± 1396
250	SPIRE *Herschel*[a]	2010	60	3805 ± 571
350	SPIRE *Herschel*[a]	2010	70	3095 ± 464
500	SPIRE *Herschel*[a]	2010	112	2992 ± 449
1153	IRAM PdB[b]	2010	–	7220 ± 1083
1303	IRAM PdB[b]	2010	–	7741 ± 1161
1428	IRAM PdB[b]	2010	–	7299 ± 1095
2710	IRAM PdB[b]	2010	–	10 000 ± 1500
2913	IRAM PdB[b]	2010	–	10 713 ± 1607
3019	IRAM PdB[b]	2010	–	10 330 ± 1550
20 675	UMRAO[e]	2010	–	23 230 ± 130

[a]This work. The errorbars correspond to the absolute flux uncertainties: 10 per cent at PACS BS and BL and 20 per cent at R, and 15 per cent at all SPIRE wavelengths; [b]Trippe et al. (2011); [c]Moshir et al. (1990); [d]Weedman et al. (2005); [e]University of Michigan Radio Astronomy Observatory data for year 2010 (courtesy of M. Aller and H. Aller).

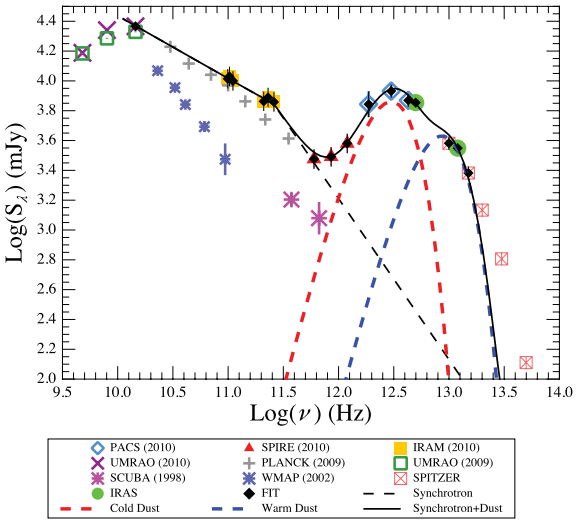

Figure 10. The SED for NGC 1275. The dust emission dominates at FIR wavelengths, whereas the AGN synchrotron emission dominates at sub-mm wavelengths. The points overlaid with black diamonds were used to find the best-fitting parameters of the model.

possibly, IR wavelengths (Krabbe et al. 2000). Hence, we preferred a broken power law, such that $|\alpha_2| > |\alpha_1|$, to an exponential term to represent the slowly decaying synchrotron emission.

Assuming the dust to be in thermal equilibrium, equation (3) quantifies the dust emission, which is a blackbody function modified by a term that depends on the dust optical depth, τ_ν, defined as

$$\tau_\nu = \kappa_\nu \frac{M_\mathrm{d}}{D_\mathrm{A}^2\,\Omega}. \quad (4)$$

The modification from a standard blackbody function is due to the fact that for typical dust temperatures, the dust grains are smaller than the peak wavelength of the Planck function and hence do not radiate as perfectly as a blackbody. Here, M_d is the dust mass, T_d is the dust temperature, $\kappa_\nu = \kappa_{\nu_0}(\nu/\nu_0)^\beta$ is the dust absorption coefficient and we adopted $\kappa_{\nu_0} = 1$ m^2 kg^{-1} at 1200 GHz (250 μm; Hildebrand 1983). β is the dust emissivity index, which based on empirical results likely lies in the range 1–2. $B_\nu(T)$ is the Planck function at frequency ν and temperature T. $B_\nu(T_\mathrm{cmb})$ is the contribution from the cosmic microwave background at $T_\mathrm{cmb} = 2.73(1+z)$ K. Ω is the solid angle subtended by the source, here assumed to be the total extent of the FIR emission at 70 μm.

The power-law indices for the AGN emission, α_1 and α_2, were constrained to have negative values, so that the synchrotron emission decreases with increasing frequency. Dunne & Eales (2001) showed that a two-component dust model with β close to 2 better fits the observed SEDs than a single-component dust model. This is also consistent with our findings based on the SEDs of CC BCGs investigated so far (Edge et al. 2010a,b; Mittal et al. 2011). We therefore fitted the data with a model comprising a cold and warm dust component parametrized by temperature and mass ($T_\mathrm{d,c}$, $M_\mathrm{d,c}$) and ($T_\mathrm{d,w}$, $M_\mathrm{d,w}$), respectively. We used the Levenberg–Marquardt non-linear least-squares fitting algorithm from Numerical Recipes to

Table 4. The best-fitting model parameters of the function describing the FIR emission (equation 1) for the dust emissivity index, $\beta = 1$. For comparison, we also give the parameters for $\beta = 1.5$ and 2. The uncertainties correspond to the 1σ errorbars.

Parameter	$\beta = 1.0$	$\beta = 1.5$	$\beta = 2.0$
Cold dust temperature, $T_{\rm d,c}$	(38.0 ± 2.0) K	(35.0 ± 1.6) K	(31.8 ± 1.3) K
Cold dust mass, $M_{\rm d,c}$	$10^{6.96\ \pm 0.12}$ M$_\odot$	$10^{6.91\ \pm 0.12}$ M$_\odot$	$10^{6.89\ \pm 0.12}$ M$_\odot$
Warm dust temperature, $T_{\rm d,w}$	(115.5 ± 8.5) K	(107.0 ± 7.4) K	(95.7 ± 6.0) K
Warm dust mass, $M_{\rm d,w}$	$10^{4.71\ \pm 0.17}$ M$_\odot$	$10^{4.37\ \pm 0.17}$ M$_\odot$	$10^{4.60\ \pm 0.18}$ M$_\odot$
Synch. power-law norm., S_0	$(10\,434 \pm 393)$ mJy	$(10\,364 \pm 393)$ mJy	$(10\,448 \pm 393)$ mJy
Synch. power-law index 1, $\alpha 1$	-0.41 ± 0.02	-0.42 ± 0.02	-0.41 ± 0.02
Synch. power-law index 2, $\alpha 2$	-1.08 ± 0.28	-0.92 ± 0.24	-0.83 ± 0.21
Synch. power-law break frequency, $\nu_{\rm break}$	$(2.6 \pm 0.5) \times 10^{11}$ Hz	$(2.6 \pm 0.6) \times 10^{11}$ Hz	$(2.5 \pm 0.7) \times 10^{11}$ Hz
Derived quantities			
Dust luminosity (8–1000 μm), $L_{\rm FIR}$	$(1.4 \pm 0.05) \times 10^{11}$ L$_\odot$	$(1.3 \pm 0.05) \times 10^{11}$ L$_\odot$	$(1.3 \pm 0.05) \times 10^{11}$ L$_\odot$
SFR	24 ± 1 M$_\odot$ yr^{-1}	23 ± 1 M$_\odot$ yr^{-1}	22 ± 1 M$_\odot$ yr^{-1}
Total gas-to-dust mass ratio	4500–7800	5000–8000	5300–9200

obtain the best-fitting model parameters appearing in equation (1): $M_{\rm d,c}$, $T_{\rm d,c}$, $M_{\rm d,w}$, $T_{\rm d,w}$, β, S_0, α_1, α_2 and $\nu_{\rm break}$. We explored a range of values between 0.5 and 2.5 for the dust emissivity index, β. The χ^2-minimization gave a best-fitting value β which was <1. Note that there is a strong degeneracy between β and the dust temperature such that all values of β explored yield models, with varying temperatures, that are compatible with the observed SED. That is, for any of the explored values of β between 0.5 and 2.5, the best-fitting χ^2 value was less than 11; for a χ^2 distribution with $17 - 8 = 9$ degrees of freedom (because we are not optimizing over β), this corresponds to a p-value (Gregory 2005) greater than 0.10, i.e. a model consistent with the data. Based on the work of Dunne & Eales (2001), however, β is expected to lie between 1 and 2, and so we fixed β to unity and found the best-fitting values for the other parameters subject to that choice.

The best-fitting model is shown in Fig. 10 (black solid line), as are the AGN (thin dashed line) and the dust contributions (thick dashed lines; red representing the cold dust component and blue representing the warm dust component). In addition to the fitted flux densities, we show the supplementary *Spitzer*/*IRAS* and UMRAO data, along with SCUBA (Irwin et al. 2001) and *Wilkinson Microwave Anisotropy Probe* (*WMAP*; Wright et al. 2009) data from around year 2000. The SCUBA (big magenta crosses) and *WMAP* data (small indigo crosses) clearly demonstrate the strong variability in the radio source and, hence, the need for coeval flux densities for SED fitting. Similarly, the Planck (grey plus symbols; Planck Collaboration et al. 2011) and UMRAO data (open green squares) from the year 2009 fall slightly below the IRAM and UMRAO data, both from the year 2010, respectively.

The best-fitting parameter values were used to calculate the total dust emissivity by integrating the emission between 8 and 1000 μm. Assuming that young ($\leq 10^8$ yr), hot stars dominate the interstellar radiation field across the UV–optical band, the SFR can be estimated using the Kennicutt relation (Kennicutt 1998). In early-type galaxies, including BCGs, the cooler emissions (>100 μm) may arise from dust heated by a passively evolving old stellar population (OSP), which warrants caution in the Kennicutt calibration. The best-fitting parameters for $\beta = 1$ and the derived quantities are given in Table 4 (we also give the best-fitting parameters for $\beta = 1.5$ and 2.0 for comparison) and the predicted dust and AGN flux contributions are given in Table 5. A total gas-to-dust mass ratio between 4500 and 7800 was estimated using the molecular gas mass $\sim 4 \times 10^{10}$ M$_\odot$ derived in Salomé et al. (2006). The total gas mass depends upon the conversion factor used to calculate the atomic plus molecular mass. We used a factor of 1.36 as given in Edge (2001). The total gas-to-dust mass ratio, although high, is within the range of the derived mass ratios in other CC BCGs (Edge 2001). At the other extreme is NGC 4696, for which a 3σ upper limit of ∼450 was obtained on the total gas-to-dust mass ratio (Mittal et al. 2011).

Table 5. Dust and AGN contributions based on the best-fitting model given in Table 4.

Wavelength (μm)	Dust (mJy)	AGN (mJy)
20	2349 ± 221	88 ± 62
25	3384 ± 163	112 ± 74
30	3890 ± 282	137 ± 85
60	6772 ± 295	289 ± 143
70	7840 ± 389	341 ± 160
100	8513 ± 775	502 ± 202
160	5532 ± 746	833 ± 265
250	2493 ± 369	1349 ± 323
350	1175 ± 171	1939 ± 354
500	485 ± 67	2850 ± 363
1153	50 ± 6	7023 ± 714
1303	35 ± 4	7389 ± 398
1428	27 ± 3	7673 ± 400
2710	4.2 ± 0.5	$10\,008 \pm 396$
2914	3.4 ± 0.4	$10\,313 \pm 394$
3019	3.1 ± 0.3	$10\,466 \pm 392$
20 675	0.0 ± 0.0	$23\,231 \pm 130$

While the SPIRE and PACS 100 μm observations were made close in time to the IRAM sub-mm observations (2010 August 24–September 9), the PACS 70 μm observations were made half a year later (2010 March 14), and so the underlying contribution from the AGN may have varied because of the variability in the AGN output. According to the best-fitting model, this is not an issue of concern since the AGN contribution to the total flux at 70 μm is small. This was also verified by discarding the 70 μm data point and refitting the data.

4 WHAT ARE THE PREVAILING HEATING MECHANISMS IN THE INNER 4 kpc OF NGC 1275?

The filamentary nebula extends out to ∼50 kpc from the core. The excitation mechanisms in the outskirts of the galaxy are very likely different from those prevailing in the core. This is evident also from

the reversal of the relative strengths of [C II] and [O I] line emission (Section 3.2) with cluster-centric distance. The core of NGC 1275, where we expect photoionization from stars and AGN to play an important role, needs to be modelled separately from the filaments. To this end, we conducted simulations using the radiative transfer code CLOUDY (Ferland et al. 1998), the main goal of which was to determine whether or not an additional form of heating is required to reproduce some of the observed emission lines emerging from the core. For example, in the case of NGC 4696, the BCG of the Centaurus cluster, the [C II]/$L_{\rm FIR}$ and Hα/[C II] ratios clearly call for another heating component, in addition to photoionization (Mittal et al. 2011).

From the point of view of energetics of a cooling plasma, earlier works, such as Johnstone et al. (1987), Heckman et al. (1989), Voit, Donahue & Slavin (1994), Jaffe & Bremer (1997) and Donahue et al. (2000), have shown that the observed filamentary emissions are far too luminous to be just due to the recombination phase of gas cooling from the ICM. The observed luminosities imply far too much cooling, with mass deposition rates inconsistent by orders of magnitude with the SFRs. While such calculations have been performed for emissions such as Hα and molecular hydrogen lines, none of the current cooling calculations simulate the FIR emission lines. This is because the existing cooling calculations (that use codes like CLOUDY, APEC, MKCFLOW) usually stop when the gas reaches a temperature of $\sim 10^4$ K, not low enough to produce the FIR lines under consideration. Hence, it is presently not possible to estimate the luminosity of the FIR lines from a simple cooling-flow plasma.

We modelled a composite cloud comprising a photodissociation region (PDR) adjacent to an ionized (H II) region. For the equation of state we assumed a constant gas pressure throughout the cloud. As input, we provided the normalization for an OSP, $\eta_{\rm OSP}$, the normalization for a young stellar population (YSP), $G0$ (in Habing units), the starting hydrogen density, n (in cm^{-3}), and the hydrogen column density, $N_{\rm H}$ (in cm^{-2}). For further details on the role played by these input parameters, we refer the reader to Mittal et al. (2011). The parameters, along with the range explored, are given in Table 8. Based on some initial investigations carried out to assess the effect of an OSP component on the output emissions, we concluded that the [C II]/$L_{\rm FIR}$ ratio can be better reconciled if an OSP component is included. An old generation of stars produces optical and UV photons that contribute to the heating of dust but not so much to the photoelectric heating of the gas. In the absence of an OSP component, the [C II]/$L_{\rm FIR}$ ratio for a given $G0$ is higher. The results, however, are not very sensitive to the presence of an OSP, except for low $G0$ ($\leq$100 Habing), but a low $G0$ is not consistent with other observed ratios, as we will show below.

We used the STARBURST99 stellar synthesis library (Leitherer et al. 1999) to model both the OSP and YSP. The main input parameters to the STARBURST99 simulations are the stellar mass and age (continuous or starburst), and the initial stellar mass function. We did not explore the range of possible values these input parameters can take – that is a subject of another detailed ongoing study (Mittal et al., in preparation). For the purpose of conducting the CLOUDY simulations described here, we fixed the age and mass of the OSP to $\sim$10 Gyr and 5×10^{11} M$_\odot$, and the age and the mass of the YSP to $\sim$2 Myr and 5×10^9 M$_\odot$, respectively. The SED corresponding to a starburst 2 Myr old is indistinguishable from the one corresponding to a continuous star formation scenario, where the oldest stars are assumed to be 2 Myr. This is because the emission in both the cases is dominated by young stars that are about 2 Myr old. Hence, the young population of stars need not have formed at the same time.

Table 6. The default ISM gas-phase chemical composition used in CLOUDY simulations. The abundances are given relative to H.

Element	$\log_{10}$ abundances (ISM)
He	−1.0088
C	−3.8222
N	−4.2010
O	−3.7171
Ne	−4.1319
Mg	−5.1215
Si	−5.7222
S	−4.7113
Cl	−7.2218
Ar	−5.7716
Fe	−6.4218

The elemental abundances were initially set to their default ISM values given in Table 6. However, X-ray observations made with *Chandra* indicate a slight drop in the central metallicity with the average value around 0.6 Z$_\odot$ (Sanders & Fabian 2007). With this in mind, we also conducted simulations with a lower metallicity, which, as shown below, indeed fit the observed ratios better. We did not include any polycyclic aromatic hydrocarbon (PAH) grains since the mid-IR spectra do not contain any PAH features (Weedman et al. 2005). Although several BCGs show strong PAH features in their IR spectra indicative of star formation (Donahue et al. 2011), there are a few, such as NGC 1275 and NGC 4696 (Kaneda, Onaka & Sakon 2005), that do not. PAH molecules are small in size and can easily be destroyed through physical sputtering or thermal evaporation (Dwek & Arendt 1992; Micelotta, Jones & Tielens 2011).

The absolute and relative strengths of the FIR and Hα lines are very important diagnostics of the various heating contributors in CC BCGs. These emission lines and their ratios relative to [C II] are listed in Table 7. We note that there is a slight offset of $\sim$3 arcsec between the peak of the [C II] emission and the radio core emission (the latter coincides with the peak of Hα emission to within $\sim$0.5 arcsec). This offset is of the order of the 1σ pointing inaccuracy of the PACS spectrometer and unlikely real. However, we estimated the FIR line fluxes for both the cases – (a) assuming the offset is not real and (b) assuming the offset is real. These cases are referred to as '[C II] core' and 'radio core, respectively. The two cases have only marginal differences in their FIR line fluxes and are compared only for the purpose of illustrating the level of uncertainty in the estimated line parameters. In the following, we used the '[C II] core' as the nominal case and used the other set of line fluxes to derive uncertainties on the line ratios.

The total FIR flux associated with the core cannot be directly estimated from fitting the SED due to insufficient resolution available beyond $\sim$160 μm. We instead used the 100 μm flux as a proxy for the total luminosity. Shown in Fig. 11 is the total FIR luminosity in the range 8–1000 μm versus the 100 μm luminosity for 7 of the 11 BCGs in the *Herschel* CC BCG sample, including NGC 1275. We considered only these here because their FIR luminosity can be determined with least uncertainty. For NGC 1275 we set $L_{\rm FIR}$ equal to the total dust luminosity. This relation is being investigated for the whole sample separately (Oonk et al., in preparation). There is a clear correlation between the total FIR luminosity and the 100 μm luminosity, such that $L_{\rm FIR} \propto L_{100\,\mu{\rm m}}^{1.09}$. The trend is also observed in the flux–flux plane (not shown), and so the correlation is not spuriously induced due to the common dependence of the two quantities

Table 7. A comparison of FIR and optical emission lines in the core region. Given in the last column are the ratios with respect to [C II]. The Hα flux has been corrected for the Galactic extinction. We also give the Hα flux after correcting for the internal extinction assuming $E(B-V) = 0.37$ in parentheses.

Region	RA	Dec.	Aperture radius (arcsec)	Line	Velocity (km s^{-1})	Flux (10^{-15} erg s^{-1} cm^{-2})	Ratio
Radio core	$03^h19^m48^s.16$	$+41°30'42''.1$	11	[C II]	11 ± 3	665.1 ± 6.3	1.00
				[O I]	27 ± 4	1310.5 ± 18.4	1.97
				[O IB]	50 ± 9	81.2 ± 2.1	0.12
				[N II]	-2 ± 7	53.7 ± 1.1	0.08
				[O III]	-26 ± 15	59.0 ± 3.1	0.09
				Hα		1810 (4185)	2.7 (6.3)
				L_{FIR}		$\sim 5.9 \times 10^5$	$\sim$800
C II core	$03^h19^m48^s.01$	$+41°30'44''.9$	11	[C II]	8 ± 3	724.8 ± 7.3	1.00
				[O I]	23 ± 4	1320.2 ± 17.3	1.82
				[O IB]	47 ± 8	84.3 ± 2.0	0.12
				[N II]	-4 ± 8	58.1 ± 1.2	0.08
				[O III]	-30 ± 14	66.1 ± 3.0	0.09
				Hα		1810 (4185)	2.5 (5.8)
				L_{FIR}		$\sim 5.9 \times 10^5$	$\sim$700

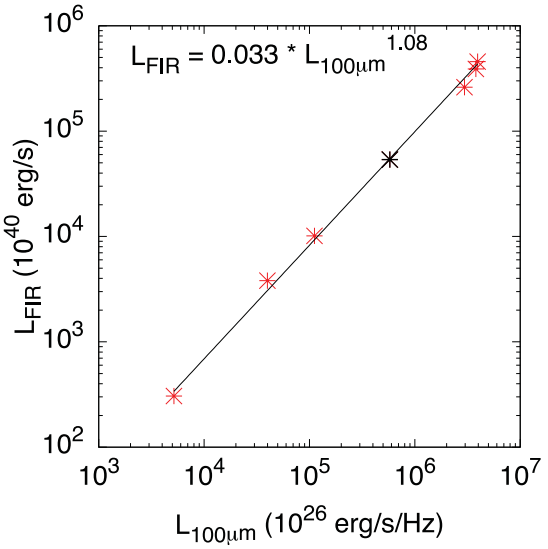

Figure 11. The total FIR luminosity (8–1000 μm) versus the 100 μm luminosity for 7 of the 11 BCGs in the *Herschel* CC BCG sample. NGC 1275 is denoted as a black cross.

on redshift. Using this correlation and the 100 μm core flux, the total FIR flux for the core may be estimated. The contribution from the AGN synchrotron emission at 100 μm is negligible (<6 per cent; see Table 5) and may be ignored.

The measured 100 μm flux within the core aperture of 11 arcsec radius is (5608 ± 7) mJy. Even though some of the flux may fall beyond the chosen aperture, necessitating an aperture correction, the factor is very small for the given radius. We determined the required aperture correction factor by assuming that the FIR emission correlates with the Hα emission. Assuming the WIYN Hα image to represent the true model for the FIR surface-brightness distribution, we convolved the Hα image with the PACS 100 μm point spread function (PSF) and estimated the aperture correction from the ratio of the flux from the smoothed image to that from the unsmoothed one. The ratio is close to unity and therefore we did not apply any aperture correction. The measured 100 μm flux yields an FIR (8–1000 μm) flux that implies an L_{FIR}/[C II] ratio ∼700–800.

4.1 Best-fitting energy model for the core

The *Herschel* FIR coolants serve as strong constraints for evaluating the physical parameters of the ISM in the BCG. Fig. 12 shows [O I]/[C II] versus n for different values of the photon parameter, $G0$. This plot can be understood in terms of the critical densities for [C II] and [O I]. This is the density at which the probabilities of collisional de-excitation and radiative de-excitation are equal (Osterbrock & Ferland 2006). Above the critical density the level populations may be considered to be in local thermal equilibrium as the level populations become dominated by collisions. The critical density is lowered by a factor that is roughly the optical depth of the line due to photon trapping when the line is optically thick. Fig. 12 shows that, for $n < n_{cr}$, the intensity of an optically thin line increases linearly with n and for $n > n_{cr}$ the intensity becomes independent of n. This result is fairly insensitive to details such as the cloud energy source, as Fig. 12 shows. While n_{cr} for [C II] is $\sim 3 \times 10^3$ cm^{-3}, it is substantially higher for [O I] $\sim 5 \times 10^5$ cm^{-3}. Therefore, at a fixed column density and photon parameter, $G0$, for high densities $3 \times 10^3 < n < 5 \times 10^5$ cm^{-3} the ratio, [O I]/[C II], continues to increase with density. This makes [O I]/[C II] a sensitive probe of density if the lines are optically thin. The individual trends displayed by the [O I] and [C II] lines in Fig. 12 are complicated by the fact that for a given column density these lines become optically thick for certain combinations of n and $G0$.

Similarly, Fig. 13 shows [N II] and [O III] versus n for different $G0$ and for two different column densities. [C II] is produced in both ionized (for e.g. H II regions) and neutral media (for e.g. PDRs); however, [N II] and [O III] are produced only in an ionized region due to their higher ionization potentials. This has the effect that [N II] and [O III] are produced profusely at the surface of the cloud facing the ionization source and reduce with the depth into the cloud. This explains the drop in both [N II] and [O III] intensities relative to [C II] with N_H. This makes [N II]/[C II] and [O III]/[C II] a sensitive probe of the cloud depth or hydrogen column density, N_H.

Of the N_H range investigated, the optimal cloud depth required to reproduce the observed ratios is 10^{23} cm^{-2}. Unless $G0$ is high (>10 000 Habing), a higher N_H does not affect the predicted ratios, implying that the cloud becomes radiation bounded. In Fig. 14, we present the modelled ratios as a function of n and $G0$ for $N_H = 10^{23}$ cm^{-2}, assuming stellar photoionization only. The

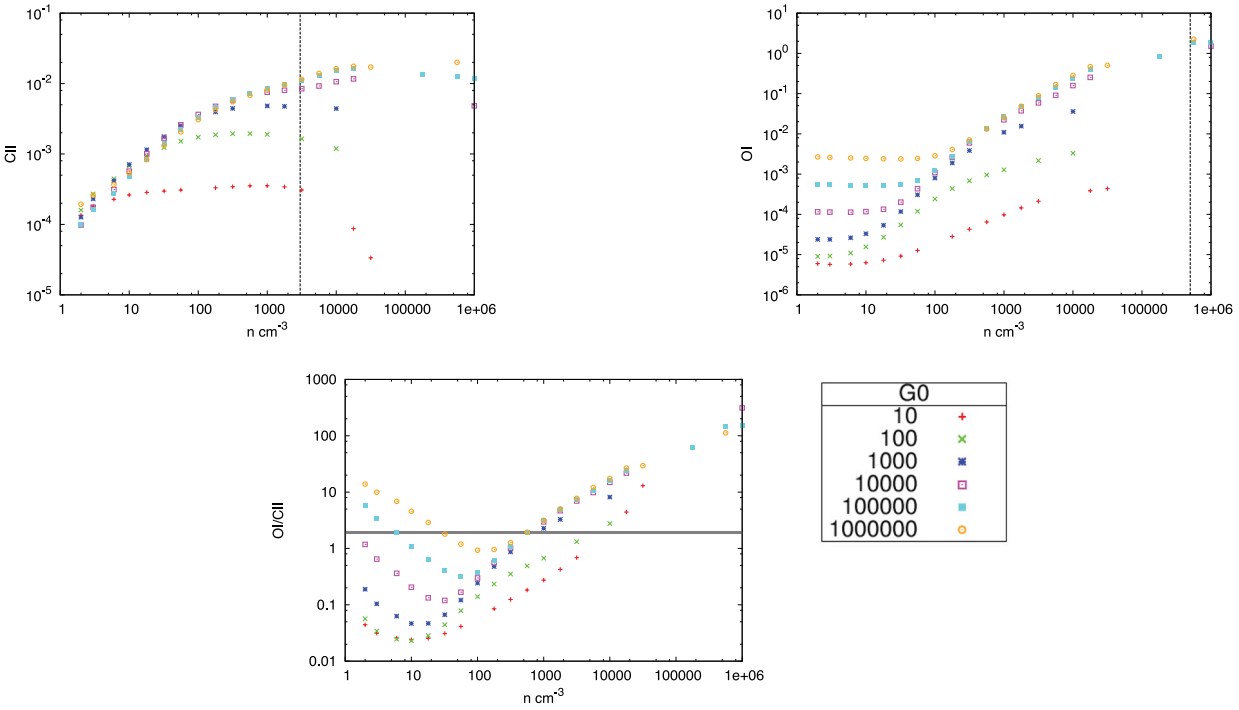

Figure 12. [O I]/[C II] sensitivity to the gas density. The simulated [C II] intensity in erg s^{-1} cm^{-2} (upper-left panel), the [O I] intensity in erg s^{-1} cm^{-2} (upper-right panel) and the [O I] to [C II] ratio (lower panel) as a function of gas density, n, and the normalization of the YSP (the photon parameter), $G0$. The column density has been fixed to $N_H = 10^{23}$ cm^{-2}. The two vertical dashed lines represent the critical densities, $n_{cr} = 3 \times 10^3$ cm^{-3} for [C II] and $n_{cr} = 3 \times 10^3$ cm^{-3} for [O I]. The horizontal solid line corresponds to the observed ratio of [O I] to [C II] for the inner 4 kpc region.

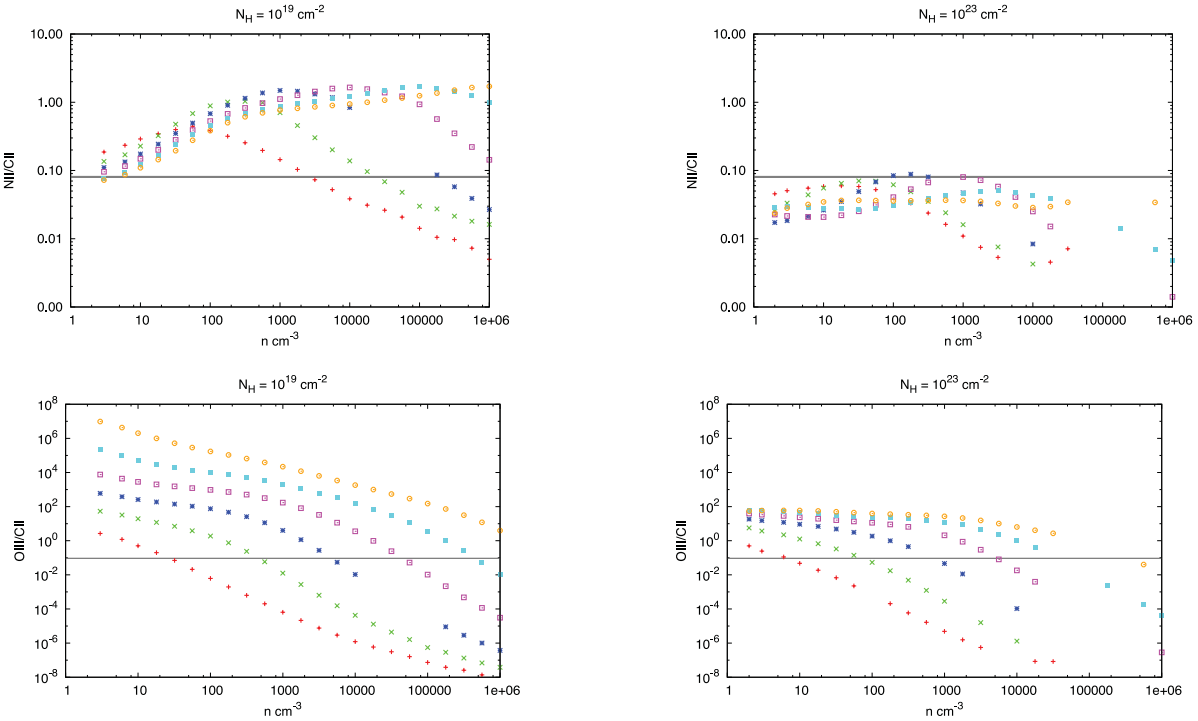

Figure 13. [N II]/[C II] (upper row) and [O III]/[C II] (lower row) versus density, n. Shown are the ratios for two different column densities, $N_H = 10^{19}$ (left) and 10^{23} cm^{-2} (right). [N II] and [O III] are produced in abundance at the surface of the cloud facing the ionization source and deplete with the depth of the cloud and, hence, sensitive probes of N_H. The different points have the same meaning as in Fig. 12. The horizontal lines represent the observed ratios in the inner 4 kpc region.

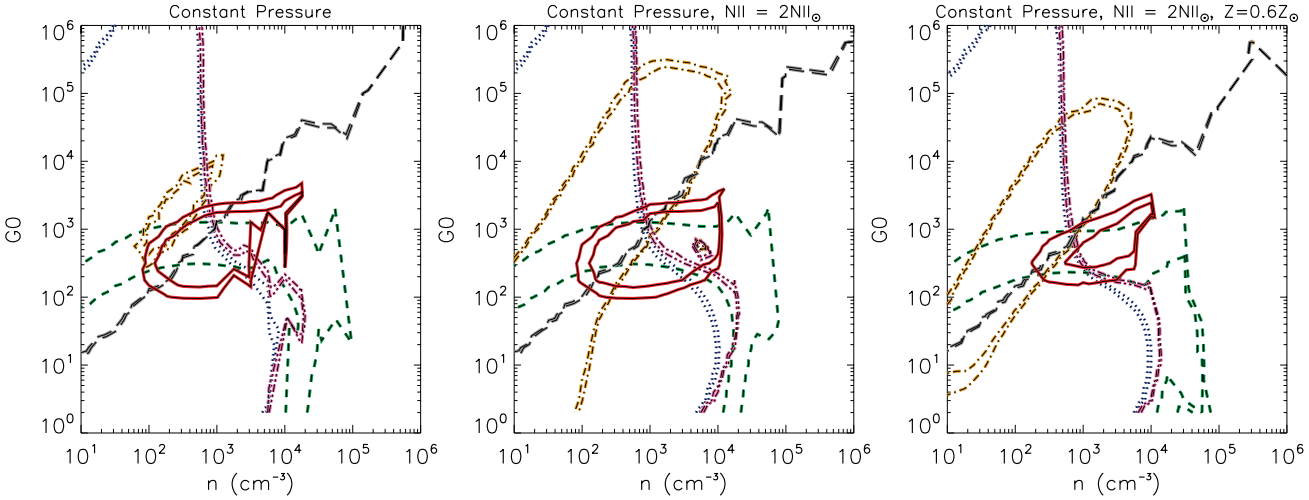

Figure 14. Simulations based on a photoionization model containing only stars. Shown are contours corresponding to the lower and upper observed limits (given in square brackets below) for $L_{\rm FIR}$/[C II] (solid red) → [700:800]; [O I]/[C II] (dotted blue) → [1.79:2.00]; Hα/[C II] (dashed green) → [2.5:6.3]; [N II]/[C II] (dot–dashed orange) → [0.078:0.082]; [O IB]/[C II] (double dot–dashed pink) → [0.113:0.125] and [O III]/[C II] (long dashed grey) → [0.083:0.095]. For this simple model, the regions allowed by the data, between the paired lines, would be expected to overlap at a single Habing flux ($G0$) and cloud density (n). Left: the element abundances are fixed to their default ISM values. Middle: nitrogen overabundance is fixed to 2. Right: the element abundances are fixed to 0.6 times the ISM value and nitrogen overabundance to 2. The best-measured ratio, $L_{\rm FIR}$/[C II], overlaps for this model.

different sets of curves correspond to the observed lower and upper limits of [C II]/$L_{\rm FIR}$ (solid red), [O I]/[C II] (dotted blue), Hα/[C II] (dashed green), [N II]/[C II] (dot–dashed orange), [O IB]/[C II] (double dot–dashed pink) and [O III]/[C II] (long dashed grey). Note that the observed Hα/[C II] ratio has a wide range due to the uncertainties mentioned in Section 2.2. The FIR ratios, in contrast, are much better constrained. Consequently, our strategy was to first try and reproduce the FIR line and continuum ratios and then use Hα/[C II] to check for consistency against the best-fitting model.

The left-hand panel of Fig. 14 assumes ISM abundances, as adopted in Ferland et al. (2008). While [O I]/[C II], [O IB]/[C II] and [O III]/[C II] converge at $n \sim 1000\,{\rm cm}^{-3}$ and $G0 \sim 1000$ Habing, the predicted [N II]/[C II] for this combination of n and $G0$ is less than the observed ratio. The middle panel of Fig. 14 assumes that the nitrogen abundance is twice the ISM value, yielding a much better convergence between the FIR ratios. Curiously, the best-fitting (n, $G0$) for NGC 4696 in the Centaurus galaxy cluster can also be reconciled with the observed [N II]/[C II] only if the nitrogen abundance is increased by a factor of 2 over the assumed overall metallicity (Mittal et al. 2011). In the case of NGC 4696, the need for an overabundance in nitrogen is confirmed by independent observations in the optical and X-ray bands. An overabundance of nitrogen could imply an abundance of intermediate-mass asymptotic giant branch stars with pre-main-sequence mass between 3 and 8 $M_\odot$, which may convert dredged-up carbon in their outer shells into nitrogen (Iben 1975; Wood, Bessell & Fox 1983). We are conducting such detailed radiative transfer modelling of all the CC BCGs in the *Herschel* sample, and it will be interesting to see if this is a generic feature of galaxies at the centre of cooling flows.

As mentioned in Section 4, X-ray observations suggest a lower metallicity in the core of Perseus ($\lesssim$20 arcsec $\sim$ 7 kpc). Hence, in the right-hand panel of Fig. 14, we show the predicted ratios for a metallicity equal to 0.6 times the ISM value. The FIR ratios coincide nicely at $n \sim 650\,{\rm cm}^{-3}$ and $G0 \sim 800$ Habing. We can now derive constraints on the physical scale of the cloud by comparing the [C II] flux emerging from the modelled cloud and the observed [C II] flux. For the range of n and $G0$ given in Table 8, the emergent [C II] flux is in the range 3.2×10^{-3}–$3.7 \times 10^{-3}\,{\rm erg\,s^{-1}\,cm^{-2}}$. The size of the cloud that produces [C II] flux at the distance of Earth between 665.1×10^{-15} and $724.8 \times 10^{-15}\,{\rm erg\,s^{-1}\,cm^{-2}}$ is $\gtrsim$1 kpc, yielding a volume filling factor of 1.7×10^{-2}.

The main conclusion from modelling the ISM associated with the core of NGC 1275 is that a stellar-like ionizing source with $G0 \sim$ 1000 Habing is capable of reproducing the observed FIR emission and Hα emission. No additional form of heating is required to explain these observations.

4.2 Consistency with optical flux ratios

According to previous studies (Johnstone & Fabian 1988; Donahue & Voit 1991; Johnstone et al. 2007; Ferland et al. 2009), a pure stellar or a pure active nucleus origin as the source of the optical filaments

Table 8. Input parameters for the CLOUDY simulations.

Parameter	Symbol	Input range	Likely values
Total hydrogen density (cm^{-3})	n	10–10^6	500–700
FUV intensity field (Habing[a])	$G0$	1–10^6	700–900
Hydrogen column density (cm^{-2})	$N_{\rm H}$	10^{19}–10^{26}	$>10^{23}$
Metallicity	Z	–	0.6
Nitrogen abundance (relative to Z)	$Z_\odot$(N)	–	2
Normalization for the OSP[b] ($10^{-16}\,{\rm erg\,s^{-1}\,cm^{-2}\,Hz^{-1}}$)	$\eta_{\rm OSP}$	–	52.54

[a]1 Habing $= 1.6 \times 10^{-3}\,{\rm erg\,s^{-1}\,cm^{-2}}$; [b]OSP: old stellar population.

Table 9. The optical emission line ratios in the central 4 kpc region of NGC 1275 (Johnstone & Fabian 1988). The columns are (1) the species, (2) the measured ratios, (3) the predicted ratios based on the best-fitting model and (4) the predicted ratios based on a slightly modified model. The observed ratios are from the observations off to the SE side of the nucleus to avoid the HVS.

Ratio	Value	Model I	Model II
[O II]λλ3727, 3729/Hβ	3.5–8	1–2	1–2
[O III]λ5007/Hβ	1.2–1.8	0.1–0.2	0.7–2
[O I]λ6300/Hα+[N II]λ6583	0.06–0.14	0.004–0.007	0.008–0.01
[N II]λ6583/Hα	0.8–1.4	0.6–0.9	0.6–0.9
[S II]λ6731/Hα	0.2–0.7	0.6–0.8	0.6–0.8

has difficulty explaining certain optical flux ratios. This may be true for the filaments but we suspect that stellar photoionization becomes increasingly important with decreasing distance to the core of the galaxy. Although fitting line and continuum ratios measured in different bands across the electromagnetic spectrum (sub-mm, IR, optical, UV) simultaneously is beyond the scope of this paper, we compared a subset of the optical ratios measured by Johnstone & Fabian (1988) to our best-fitting model predictions. This comparison is shown in Table 9. We give a range for the observed ratios since the ratios display a strong radial gradient. 'Model I' refers to the best-fitting energy model described above. While the predicted values of the [N II]λ6583/Hα and [S II]λ6731/Hα ratios are consistent with the observed values, [O II]λλ3727, 3729/Hβ is lower by a factor of a few and [O III]λ5007/Hβ and [O I]λ6300/[N II]λ6583+Hα are lower by about an order of magnitude than the observed values. We devised another model, referred to as 'Model II', obtained by slightly modifying the best-fitting model by decreasing the age of the input YSP by an order of magnitude. Using Model II we are able to reproduce some of the optical ratios, specifically, the ratio [O III]/Hβ. There is also an increase in the ratio, [O I]λ6300/[N II]λ6583+Hα, by a factor of 2. The modified model does not impact the best-fitting model parameters constrained by the relative strengths of FIR and Hα lines (Table 7). This is due to the fact that lowering the age of the oldest stars in the YSP alters the SED only below 1000 Å, such that [O III]λ5007 and [O I]λ6300 are affected. FIR lines, on the other hand, are mainly produced by gas heated by lower energy UV and optical photons.

From this exercise we conclude that photoionization from stars is the predominant source of energy in the cold gas clouds in the core of NGC 1275. It may be that in order to obtain consistency with the complete set of observed flux ratios at different wavebands, a composite model that includes a stellar component and one or more additional forms of heating is required. Particle-heating models are usually very hard to distinguish from slow shocks (e.g. Ferland et al. 2008; Farage et al. 2010; Rich, Kewley & Dopita 2011). Even though the work of Ferland et al. (2009) showed that ionizing particles are the likely heating agents in the filaments of NGC 1275, the particle-heating model was only marginally more successful than heating by dissipative magnetohydrodynamic (MHD) wave energy. The core of NGC 1275 displays large-scale motions, which may very well entail shocks (although strong shocks have been ruled out by X-ray data; Fabian et al. 2003; Sanders & Fabian 2007). Similarly, due to the proximity to the AGN, particle heating (cosmic rays) may be significant as well. Hence, additional heating required to explain the FIR and optical line ratios in entirety may either manifest itself in the form of weak shocks or particle heating or both.

4.3 Star formation

FUV emission is a direct indicator of the morphological and spatial extent of recent star formation sites. In Fig. 15, we show the FUV emission associated with the BCG of Perseus. This image was created using two data sets from the *HST* archive – (1) Space Telescope Imaging Spectrograph (STIS) FUV-MAMA/F25SRF2 data (proposal ID: 8107; PI: C. O'Dea) and (2) ACS Solar Blind Channel (ACS/SBC) FUV-MAMA/F140LP data (proposal ID: 11207; PI: R. O'Connell). The first data set consisted of a single pointing only (centred on the core). The second data set, however, consisted of eight different pointings, designed to map the bright UV filaments extending NW and SE from the core. We obtained the single flat-fielded, dark-subtracted exposures from the *HST* archive for both the data sets and combined them using the IRAF task, MULTIDRIZZLE.

The filaments NW of the core have the same spiral morphology as the HVS. This spatial correlation seems to suggest that the star clusters in the filaments are associated with the foreground galaxy (e.g. Keel & White 2001). There is also evidence to the contrary, suggesting that the star clusters belong to the LVS (e.g. Goudfrooij 1995; Brodie et al. 1998).

For this study, we will focus only on the FUV emission originating from the core region (see Fig. 16), which, due to proximity and symmetry, is expected to be associated with the LVS. The integrated flux density within the core is $(5.3 \pm 0.1) \times 10^{-15}$ erg s^{-1} cm^{-2} Å^{-1} at 1456 Å; however, the FUV emission close to the centre is likely to be associated with the AGN. For the purpose of quantifying FUV emission from stars, we determined the FUV emission in the annulus (0.5–3.8 kpc) as $(3.6 \pm 0.1) \times 10^{-15}$ erg s^{-1} cm^{-2} Å^{-1}, and correcting for the Galactic extinction results in $(1.2 \pm 0.3) \times 10^{-14}$ erg s^{-1} cm^{-2} Å^{-1}. There is a further correction factor that needs to be applied in order to account for the dust internal to the

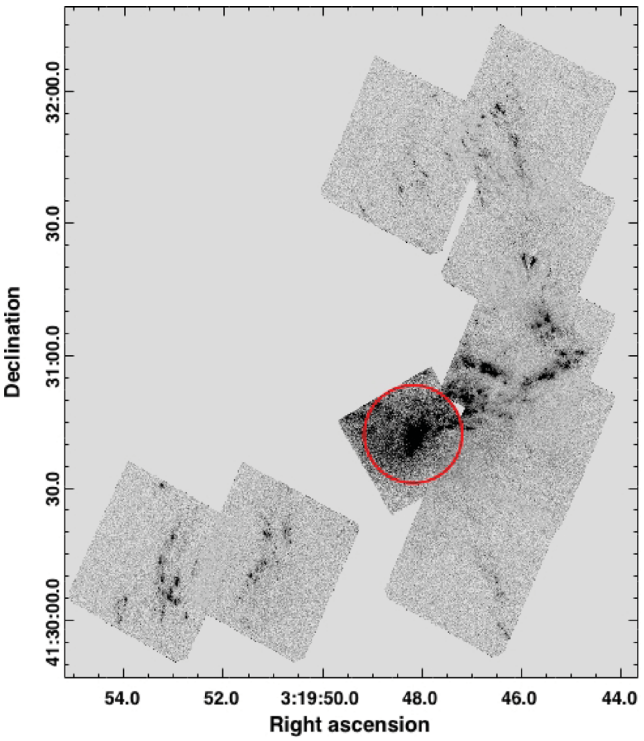

Figure 15. Combined *HST* SBC/F140LP and STIS/F25SRF2 FUV image of NGC 1275. The red circle indicates the central 4 kpc core region.

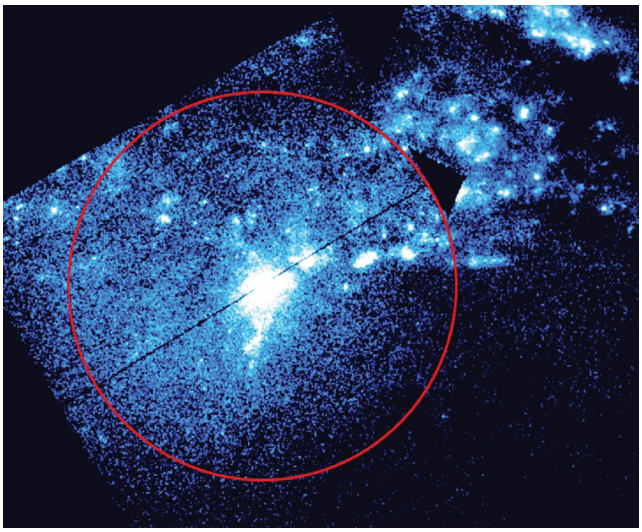

Figure 16. A zoom-in FUV image of the centre of the galaxy; the red circle indicates the central 4 kpc core region.

ISM of NGC 1275 (see Section 2.3). Assuming an internal reddening of $E(B-V) = 0.37$, we obtain an FUV flux density of $(1.9 \pm 0.5) \times 10^{-13}$ erg s^{-1} cm^{-2} Å^{-1}. This can be directly compared to the flux density expected from a synthetic spectrum of a YSP, such as the one used as input for the CLOUDY simulations. The expected flux density was determined by convolving the redshifted synthetic spectrum with the bandpass of the FUV-MAMA/F25SRF2 filter on STIS using the IRAF tool SYNPHOT. A synthetic spectrum corresponding to an instantaneous starburst containing 5×10^9 M$_\odot$ and 2 Myr in age predicts a flux density of 1.7×10^{-11} erg s^{-1} cm^{-2} Å^{-1}. Holding the age constant and scaling down the mass so that the flux density agrees with the extinction-corrected observed flux density implies an SFR of 27 M$_\odot$ yr^{-1}. This is similar to the SFR $\sim$ 24 M$_\odot$ yr^{-1} derived in Section 3.3 (Table 4) from the FIR measurements. This is also in very good agreement with the SFR $\sim$ 25 M$_\odot$ yr^{-1} derived by Norgaard-Nielsen, Hansen & Jorgensen (1990) from the *IUE* (*International Ultraviolet Explorer*) spectroscopic data.

Since the SFR traced via FIR data is expected to be most accurate (due to negligible extinction at FIR wavelengths), and the FUV rate matches it, the average internal reddening over the inner 4 kpc radius region is probably close to that suggested by the observed Galactic-extinction corrected Balmer decrement (4.07) in a region 18 arcsec SW of the nucleus (Section 2.3). On the other hand, the SFR derived above using FUV data is for the core region, whereas the SFR derived in Table 4 is for the whole galaxy. For example, Canning et al. (2010) obtained an optical SFR of about 20 M$_\odot$ yr^{-1} over the Blue Loop region, which is outside the core region. Although there is hardly any FIR emission detected in the Blue Loop region, it is possible that it contributes to the total SFR derived from FIR measurements to some extent. This could imply that the average internal reddening over the core is lower than assumed, making the FUV-derived SFR lower as well. Hence, $E(B-V) \sim 0.37$ is an upper limit. Note that the above calculation is based on two assumptions: (1) the dust in NGC 1275 follows the same extinction law as the Milky Way and (2) the Balmer line ratios are close to the case-B recombination values.

It is interesting that if we use the dust attenuation derived from the Balmer decrement and apply it at smaller (UV) wavelengths, the FIR- and UV-derived SFRs are consistent with each other. This is in contrast to studies that have indicated that the reddening values diverge between nebular line emission and UV continuum by a factor of 2 (e.g. Calzetti 1997; Buat et al. 2002), such that nebular lines, like Hα and Hβ, are more attenuated than the stellar continuum emission. This discrepancy is usually attributed to an uneven distribution of dust in front of stars and ionized gas, with the latter being more closely associated with the dust than the former. Calzetti (1997) suggests using the relation $E(B-V)_{\rm star} = 0.44 \times E(B-V)_{\rm gas}$. However, Garn et al. (2010) argue that the while the continuum at longer wavelengths (optical) may be probing older stellar population residing in less dusty environments, and hence may not be co-spatial with the ionized gas, the continuum at shorter wavelengths (UV) should be more closely tied to the young stars producing ionized gas. Hence, the correction factor (0.44) for FUV emission may be higher than suggested by the above relation.

Using the relation suggested by Calzetti (1997), Buat et al. (2002) derived $A_{\rm UV(\lambda=2000)} = 1.6 \times A_{\rm H\alpha}$. Instead of applying the attenuation at FUV wavelengths by extrapolating the reddening value calculated from the Balmer decrement, if we apply the above calibration we obtain an SFR of 6 M$_\odot$ yr^{-1}. This is a factor of 4 lower than the FIR-derived SFR. This implies that in the case of NGC 1275, the dust covering factor for the ionized gas resulting in the Balmer lines and the FUV emission must be rather homogeneous, such that the attenuation tracked by the ionized gas is closely related to that of the FUV emission.

5 DISCUSSION OF THE OUTER FILAMENTS

Ferland et al. (2009, F09 hereafter) conducted a thorough analysis of the Horseshoe region in NGC 1275. They used the IR and optical line intensities to distinguish between two types of heating: extra heating, as would be produced by passing shocks, and heating by energetic particles such as cosmic rays. Extra heating refers to heating by dissipative MHD waves, and it is assumed that this kind of heating increases the thermal energy of the gas only. Hence, the local gas kinetic temperature dictates the collisional processes that are energetically possible. Energetic particle heating refers essentially to ionizing particles, and, on the other hand, is not only capable of depositing thermal energy via elastic collisions with the particles of the ISM but can also ionize a neutral medium via creation of a population of suprathermal secondary electrons. The physics of molecular gas exposed to such heating sources is described by Ferland (2011, 2012).

The model in F09 assumes that the gas in the filaments is in pressure balance with the surrounding X-ray-emitting intracluster gas. Based on the X-ray measurement of the electron pressure of 0.128 keV cm^{-3} of the hot gas surrounding the horseshoe by Sanders & Fabian (2007), F09 assumed a constant pressure of $nT = 10^{6.5}$ cm^{-3} K. The simulations conducted in F09 are further based on the assumption that the filaments are composed of cloudlets with a range of density, n, and temperature, T, but which have this single pressure, nT. This assumption is motivated by the fact that ionic, atomic and molecular emissions are all observed in the filaments. This implies that different phases of gas occupy a telescope beam, even at *HST* resolution. In other words, there is observational evidence that both dense molecular and diffuse ionized emission arise from spatially coincident regions. Because of the constant pressure assumption, low-density cloudlets have high temperature and produce emission from ionized gas, while dense clouds are cold and account for the molecular component.

The formalism adopted in F09 uses a cumulative filling factor $f(n)$, which is a power law in density, as the weighting function to co-add clouds of different densities. This factor describes the

fractional volume filled with gas with density n or lower. The spectra for various emission lines, in particular the IR H_2 and optical H I emission lines, are determined using CLOUDY using a range of electron densities, temperatures and non-radiative heating rates. The emission for a given line is integrated over the ensemble of clouds and then compared to observations.

F09 found that both the forms of non-radiative heating, extra heating and energetic particle heating, match the optical and IR observations to within a factor of 2 for the majority of the lines. There are a few discriminant lines, such as the optical emission lines He I λ 5876 Å, [Ne III] λ 3869 Å and the IR emission line [Ne II] λ 12.81 μm, which show a few orders of magnitude difference and indicate that ionizing particles are responsible for heating and ionizing the gas. Fabian et al. (2011) argue that the surrounding hot ICM is the source of the ionizing particles, rather than true cosmic rays as would be found in the adjoining radio lobes.

All of the predicted lines used to compare with observations were optically thin, so their intensity relative to similar forbidden lines has no dependence on cloud column density. The F09 model also made predictions for the FIR emission lines, such as those observed by *Herschel*. In Table 10, we list the detected *Herschel* emissions in the three regions of the extended filaments – the Horseshoe region, the SW knots. We also give the 3σ upper limits for the non-detections. These lines may be used to distinguish between the two heating scenarios. In particular, the predicted [O I]/[C II] ratio is ∼3 for the extra heating and ∼21 for the energetic particle heating. The observed [O I]/[C II] ratios, on the other hand, have an upper limit of 1.64 in the Horseshoe knot and 0.85 in both the SW and Blue Loop knots. This discrepancy was first pointed out by Mittal et al. (2011) in a different context.

There are two plausible explanations for why the F09 model fails to reproduce the *Herschel* observations. The first reason is tied to the critical densities, n_{cr}, of [C II] and [O I] gas (see Fig. 12). Since the F09 model assumes a constant pressure of $nT = 10^{6.5}\,\mathrm{cm^{-3}\,K}$, the FIR lines which are produced at low temperatures (∼100 K to a few hundred K) correspond to high densities ($3 \times 10^4 > n > 5 \times 10^3\,\mathrm{cm^{-3}}$). Such high densities lead to high [O I]/[C II] ratios due to the reasons given in Section 4.1. The model could be brought into agreement with the observations by postulating a large component of low-density gas, which would strongly emit the *Herschel* lines with the observed ratio. F09 note, in section 7, point 7, that large reservoirs of cold gas could be present yet not detected with the selection of lines they had available.

The second likely cause for the incompatibility of the F09 model with the [O I]/[C II] ratio is that the F09 model assumes that the emission lines are optically thin. If the gas has high enough column density, the *Herschel* lines become optically thick. This is normally the case in galactic PDRs (Tielens & Hollenbach 1985). The line luminosity is no longer determined simply by the product of the line emissivity and the volume of the cloud but rather the geometry of the emitting cloud, especially its column density, will affect the line intensities. F09 note that the observed surface brightness of the Hα line gives the line-of-sight thickness of the cloud $\mathrm{d}l \sim 0.3$ pc. This implies a hydrogen column density of $N_H = 10^{22.5}\,\mathrm{cm^{-2}}$. If the emission forms in a single cloud with this column density, the *Herschel* lines would be strongly affected but there would be little impact on the NIR and optical lines, other than the effects of internal reddening.

Clearly much remains to be learned about the geometry of the filaments at sub-*HST* resolution scales. Both scenarios outlined here are consistent with what is known from available observations.

6 CONCLUSIONS

We have presented FIR *Herschel* observations of the centre of the Perseus galaxy cluster. The BCG, NGC 1275, is surrounded by filaments, previously imaged extensively in Hα and CO emission. In this work, we report the presence of coolants, such as [C II], [O I], [N II], [O IB] and [O III], in addition to Hα and CO. All the *Herschel* lines except [O III] are spatially extended, with [C II] extending up to 25 kpc from the nucleus of the galaxy, and co-spatial with Hα and CO. Furthermore, [C II] shows a similar velocity distribution to CO, and the latter has been shown in previous studies to display a close association with the Hα kinematics. The spatial and kinematical correlation among [C II], Hα and CO gives us confidence that the different components of the gas may be modelled with a common heating model.

The velocity structure inferred from [C II] observations reveals blueshifted components on either side of the nucleus and a ridge of redshifted gas passing through the centre in the north–south direction. A combination of disc rotation on ∼10 kpc scales and more disordered motion of a few distinct clouds at larger radii is one plausible scenario consistent with [C II] (*Herschel*) and CO data. It may also be that outflows from the radio source at the centre are dredging up cold material away from the line of sight, resulting in a ridge of redshifted gas.

We have detected continuum emission at all PACS and SPIRE wavelengths ranging from 70 to 500 μm. The *Herschel* continuum data combined with a suite of existing radio, sub-mm and IR data, have allowed us to perform an SED fitting using a model comprising two modified-blackbody dust components, dominant at IR wavelengths, and synchrotron AGN emission, dominant at radio

Table 10. A comparison of [C II], [O I] and Hα line fluxes in the Horseshoe knot, the SW1/SW2 knots and the Blue Loop knots. Given in the last column are the ratios with respect to [C II]. [O I] is not detected in any of the extended filaments – we give the 3σ upper limits.

Region	RA	Dec.	Aperture radius (arcsec)	Line	Velocity (km s^{-1})	Flux (10^{-15} erg s^{-1} cm^{-2})	Ratio
Horseshoe knot	$03^h19^m45\overset{s}{.}15$	$+41°31'33\overset{''}{.}1$	11	[C II]	79.5	26.78 ± 0.26	1.00
				[O I]		<44	<1.64
				Hα		36 (88)	1.34 (3.27)
SW knots (southern filament)	$03^h19^m45\overset{s}{.}48$	$+41°29'49\overset{''}{.}4$	11	[C II]	3.3	40.67 ± 3.55	1.00
				[O I]		<34	<0.84
				Hα		87 (211)	2.14 (5.19)
Blue Loop knots (SE filament)	$03^h19^m50\overset{s}{.}72$	$+41°30'07\overset{''}{.}2$	11	[C II]	−224.5	35.19 ± 1.87	1.00
				[O I]		<30	<0.85
				Hα		73 (177)	2.07 (5.03)

and sub-mm wavelengths. The total IR luminosity (8–1000 μm) is $(1.5 \pm 0.05)10^{11}\,L_{\odot}$, making NGC 1275 a luminous IR galaxy. The IR-inferred SFR is about $24\,M_{\odot}\,yr^{-1}$. This is comparable to the SFR estimated in a core region (∼4 kpc in radius) using the *HST*-FUV observations and also *XMM–Newton* RGS observations, which suggest a residual cooling rate of $20\,M_{\odot}\,yr^{-1}$.

We have investigated in detail the source of the emissions emerging from a core region 4 kpc in radius. This investigation was done by carrying out radiative transfer simulations assuming a photoionization model consisting of only OSPs and YSPs as heating agents. We find that the *Herschel* and Hα emissions can be reproduced by such a model, yielding hydrogen density between 500 and 700 cm^{-3} and FUV intensity field between 700 and 900 Habings. Optical flux ratios indicate that a second heating component may be needed; however, stellar photoionization seems to be the dominant mechanism.

We have also detected [C II] in three previously well-studied regions of the filaments: the Horseshoe, Blue Loop and SW knots. The observed upper limits of the [O I]/[C II] ratio are 1 dex smaller than predicted by the best-fitting model of F09, wherein two sources of ionization have been considered individually: particle heating and extra heating (the latter increases the thermal energy of the gas). The [C II] line has a excitation potential of 91 K and a critical density much lower than the lines considered in that study. This suggests that the lines are optically thick, as is typical of galactic PDRs, and implies that there is a large reservoir of cold atomic gas. This has not been included in previous inventories of the filament mass and may represent a significant component. It seems likely that the model used by F09 needs to be augmented in order to reproduce the observed strengths of the various emissions in the filaments of NGC 1275. It can also be that a composite model, like the one used for the study of Centaurus (Mittal et al. 2011), consisting of more than one heating agent, is required to achieve compatibility with observations.

ACKNOWLEDGMENTS

We thank Christopher Conselice for providing the WIYN Hα image and Greg Taylor for the radio images. We thank the referee sincerely for a very useful feedback. This work is based (in part) on observations made with *Herschel*, a European Space Agency Cornerstone Mission with significant participation by NASA. This work was supported by NASA through an award issued by JPL/Caltech. We thank M. Aller for providing us with the UMRAO data. This research has made use of data from the University of Michigan Radio Astronomy Observatory which has been supported by the University of Michigan and by a series of grants from the National Science Foundation, most recently AST-0607523. This research has made use of the NASA/IPAC Extragalactic Database (NED) which is operated by the Jet Propulsion Laboratory, California Institute of Technology, under contract with the National Aeronautics and Space Administration. This work is supported in part by the Radcliffe Institute for Advanced Study at Harvard University. GJF acknowledges support by NSF (0908877; 1108928 and 1109061), NASA (10-ATP10-0053, 10-ADAP10-0073 and NNX12AH73G), JPL (RSA No 1430426), and STScI (HST-AR-12125.01, GO-12560 and HST-GO-12309). STSDAS is a product of the Space Telescope Science Institute, which is operated by AURA for NASA. HRR thanks the Canadian Space Agency Space Science Enhancement Program for support.

REFERENCES

Böhringer H., Voges W., Fabian A. C., Edge A. C., Neumann D. M., 1993, MNRAS, 264, L25
Brauher J. R., Dale D. A., Helou G., 2008, ApJS, 178, 280
Bregman J. N., Fabian A. C., Miller E. D., Irwin J. A., 2006, ApJ, 642, 746
Brodie J. P., Schroder L. L., Huchra J. P., Phillips A. C., Kissler-Patig M., Forbes D. A., 1998, AJ, 116, 691
Buat V., Boselli A., Gavazzi G., Bonfanti C., 2002, A&A, 383, 801
Calzetti D., 1997, AJ, 113, 162
Canning R. E. A., Fabian A. C., Johnstone R. M., Sanders J. S., Conselice C. J., Crawford C. S., Gallagher J. S., Zweibel E., 2010, MNRAS, 405, 115
Cardelli J. A., Clayton G. C., Mathis J. S., 1989, ApJ, 345, 245
Chapman S. C., Scott D., Borys C., Fahlman G. G., 2002, MNRAS, 330, 92
Conselice C. J., Gallagher J. S., III, Wyse R. F. G., 2001, AJ, 122, 2281
Crawford C. S., Allen S. W., Ebeling H., Edge A. C., Fabian A. C., 1999, MNRAS, 306, 857
Crawford C. S., Hatch N. A., Fabian A. C., Sanders J. S., 2005, MNRAS, 363, 216
Dhawan V., Kellermann K.-I., Romney J. D., 1998, ApJ, 498, L111
Donahue M., Voit G. M., 1991, ApJ, 381, 361
Donahue M., Voit G. M., 1993, ApJ, 414, L17
Donahue M., Mack J., Voit G. M., Sparks W., Elston R., Maloney P. R., 2000, ApJ, 545, 670
Donahue M., de Messières G. E., O'Connell R. W., Voit G. M., Hoffer A., McNamara B. R., Nulsen P. E. J., 2011, ApJ, 732, 40
Dunne L., Eales S. A., 2001, MNRAS, 327, 697
Dwek E., Arendt R. G., 1992, ARA&A, 30, 11
Edge A. C., 2001, MNRAS, 328, 762
Edge A. C., Ivison R. J., Smail I., Blain A. W., Kneib J.-P., 1999, MNRAS, 306, 599
Edge A. C., Wilman R. J., Johnstone R. M., Crawford C. S., Fabian A. C., Allen S. W., 2002, MNRAS, 337, 49
Edge A. C. et al., 2010a, A&A, 518, L46
Edge A. C. et al., 2010b, A&A, 518, L47
Egami E., Rieke G. H., Fadda D., Hines D. C., 2006, ApJ, 652, L21
Fabian A. C., 1994, ARA&A, 32, 277
Fabian A. C. et al., 2000, MNRAS, 318, L65
Fabian A. C., Sanders J. S., Allen S. W., Crawford C. S., Iwasawa K., Johnstone R. M., Schmidt R. W., Taylor G. B., 2003, MNRAS, 344, L43
Fabian A. C., Sanders J. S., Taylor G. B., Allen S. W., Crawford C. S., Johnstone R. M., Iwasawa K., 2006, MNRAS, 366, 417
Fabian A. C., Johnstone R. M., Sanders J. S., Conselice C. J., Crawford C. S., Gallagher J. S., III, Zweibel E., 2008, Nat, 454, 968
Fabian A. C., Sanders J. S., Williams R. J. R., Lazarian A., Ferland G. J., Johnstone R. M., 2011, MNRAS, 417, 172
Farage C. L., McGregor P. J., Dopita M. A., Bicknell G. V., 2010, ApJ, 724, 267
Ferland G., 2011, in Colpi M., Gallo L., Grupe D., Komossa S., Leighly K., Mathur S., eds, Proc. Sci., Narrow-Line Seyfert 1 Galaxies and Their Place in the Universe. SISSA, Trieste, PoS(NLS1)013
Ferland G. J., 2012, in Aggarwal K., Shearer F., eds, AIP Conf. Ser. Vol. 1438, Powering the Intracluster Filaments in Cool-Core Clusters of Galaxies. Am. Inst. Phys., New York, p. 124
Ferland G. J., Korista K. T., Verner D. A., Ferguson J. W., Kingdon J. B., Verner E. M., 1998, PASP, 110, 761
Ferland G. J., Fabian A. C., Hatch N. A., Johnstone R. M., Porter R. L., van Hoof P. A. M., Williams R. J. R., 2008, MNRAS, 386, L72
Ferland G. J., Fabian A. C., Hatch N. A., Johnstone R. M., Porter R. L., van Hoof P. A. M., Williams R. J. R., 2009, MNRAS, 392, 1475 (F09)
Garn T. et al., 2010, MNRAS, 402, 2017
Gitti M., Brunetti G., Setti G., 2002, A&A, 386, 456
Gitti M., Nulsen P. E. J., David L. P., McNamara B. R., Wise M. W., 2011, ApJ, 732, 13
Goudfrooij P., 1995, PASP, 107, 502
Gregory P. C., 2005, Bayesian Logical Data Analysis for the Physical Sciences. Cambridge Univ. Press, Cambridge

Griffin M. J. et al., 2010, A&A, 518, L3
Hatch N. A., Crawford C. S., Fabian A. C., Johnstone R. M., 2005, MNRAS, 358, 765
Hatch N. A., Crawford C. S., Johnstone R. M., Fabian A. C., 2006, MNRAS, 367, 433
Heckman T. M., Baum S. A., van Breugel W. J. M., McCarthy P., 1989, ApJ, 338, 48
Hicken M., Wood-Vasey W. M., Blondin S., Challis P., Jha S., Kelly P. L., Rest A., Kirshner R. P., 2009, ApJ, 700, 1097
Hildebrand R. H., 1983, QJRAS, 24, 267
Iben I., Jr, 1975, ApJ, 196, 525
Irwin J. A., Stil J. M., Bridges T. J., 2001, MNRAS, 328, 359
Jaffe W., Bremer M. N., 1997, MNRAS, 284, L1
Johnstone R. M., Fabian A. C., 1988, MNRAS, 233, 581
Johnstone R. M., Fabian A. C., Nulsen P. E. J., 1987, MNRAS, 224, 75
Johnstone R. M., Hatch N. A., Ferland G. J., Fabian A. C., Crawford C. S., Wilman R. J., 2007, MNRAS, 382, 1246
Kaneda H., Onaka T., Sakon I., 2005, ApJ, 632, L83
Keel W. C., White R. E., III, 2001, AJ, 121, 1442
Kennicutt R. C., Jr, 1998, ARA&A, 36, 189
Kent S. M., Sargent W. L. W., 1979, ApJ, 230, 667
Krabbe A., Sams B. J., III, Genzel R., Thatte N., Prada F., 2000, A&A, 354, 439
Laine S., van der Marel R. P., Lauer T. R., Postman M., O'Dea C. P., Owen F. N., 2003, AJ, 125, 478
Leitherer C. et al., 1999, ApJS, 123, 3
Lim J., Ao Y., Dinh-V-Trung, 2008, ApJ, 672, 252
Lim J., Ohyama Y., Chi-Hung Y., Dinh-V-Trung, Shiang-Yu W., 2012, ApJ, 744, 112
McDonald M., Veilleux S., Rupke D. S. N., Mushotzky R., 2010, ApJ, 721, 1262
McNamara B. R., Wise M., Sarazin C. L., Jannuzi B. T., Elston R., 1996, ApJ, 466, L9
Micelotta E. R., Jones A. P., Tielens A. G. G. M., 2011, A&A, 526, A52
Mittal R. et al., 2011, MNRAS, 418, 2386
Moshir M. et al., 1990, BAAS, 22, 1325
Nagai H. et al., 2012, MNRAS, 423, L122
Norgaard-Nielsen H. U., Hansen L., Jorgensen H. E., 1990, A&A, 240, 70
O'Dea C. P. et al., 2008, ApJ, 681, 1035
Oonk J. B. R., Hatch N. A., Jaffe W., Bremer M. N., van Weeren R. J., 2011, MNRAS, 414, 2309
Osterbrock D. E., Ferland G. J., 2006, Astrophysics of Gaseous Nebulae and Active Galactic Nuclei. University Science Books, Mill Valley, CA
Ott S., 2010, in Mizumoto Y., Morita K.-I., Ohishi M., eds, ASP Conf. Ser. Vol. 434, The Herschel Data Processing System – HIPE and Pipelines – Up and Running Since the Start of the Mission. Astron. Soc. Pac., San Francisco, p. 139
Pedlar A., Ghataure H. S., Davies R. D., Harrison B. A., Perley R., Crane P. C., Unger S. W., 1990, MNRAS, 246, 477
Pereira M. J. et al., 2010, A&A, 518, L40
Pilbratt G. L. et al., 2010, A&A, 518, L1
Pinkney J. et al., 1996, ApJ, 468, L13
Planck Collaboration et al., 2011, A&A, 536, A7
Poglitsch A. et al., 2010, A&A, 518, L2
Privon G. C., Baum S. A., O'Dea C. P., Gallimore J., Noel-Storr J., Axon D. J., Robinson A., 2012, ApJ, 747, 46
Rawle T. D. et al., 2012, ApJ, 747, 29
Revaz Y., Combes F., Salomé P., 2008, A&A, 477, L33
Rich J. A., Kewley L. J., Dopita M. A., 2011, ApJ, 734, 87
Salomé P. et al., 2006, A&A, 454, 437
Salomé P., Combes F., Revaz Y., Edge A. C., Hatch N. A., Fabian A. C., Johnstone R. M., 2008, A&A, 484, 317
Salomé P., Combes F., Revaz Y., Downes D., Edge A. C., Fabian A. C., 2011, A&A, 531, A85
Sanders J. S., Fabian A. C., 2007, MNRAS, 381, 1381
Sanders J. S., Fabian A. C., Dunn R. J. H., 2005, MNRAS, 360, 133
Simionescu A., Werner N., Finoguenov A., Böhringer H., Brüggen M., 2008, A&A, 482, 97
Simionescu A., Werner N., Forman W. R., Miller E. D., Takei Y., Böhringer H., Churazov E., Nulsen P. E. J., 2010, MNRAS, 405, 91
Sparks W. B., Macchetto F., Golombek D., 1989, ApJ, 345, 153
Sparks W. B. et al., 2012, ApJ, 750, L5
Taylor G. B., Sanders J. S., Fabian A. C., Allen S. W., 2006, MNRAS, 365, 705
Tielens A. G. G. M., Hollenbach D., 1985, ApJ, 291, 722
Tremblay G. R. et al., 2012a, MNRAS, 424, 1026
Tremblay G. R. et al., 2012b, MNRAS, 424, 1042
Trippe S. et al., 2011, A&A, 533, A97
Vermeulen R. C., Readhead A. C. S., Backer D. C., 1994, ApJ, 430, L41
Voit G. M., Donahue M., 1995, ApJ, 452, 164
Voit G. M., Donahue M., 2011, ApJ, 738, L24
Voit G. M., Donahue M., Slavin J. D., 1994, ApJS, 95, 87
Weedman D. W. et al., 2005, ApJ, 633, 706
Wilman R. J., Edge A. C., Johnstone R. M., 2005, MNRAS, 359, 755
Wood P. R., Bessell M. S., Fox M. W., 1983, ApJ, 272, 99
Wright E. L. et al., 2009, ApJS, 180, 283

This paper has been typeset from a TEX/LATEX file prepared by the author.